

## Abstract

A common assumption in satellite imager-based cirrus retrieval algorithms is that the radiative properties of a cirrus cloud may be represented by those associated with a specific ice crystal shape (or habit) and a single particle size distribution. However, observations of cirrus clouds have shown that the shapes and sizes of ice crystals may vary substantially with height within the clouds. In this study we investigate the sensitivity of the top-of-atmosphere bidirectional reflectances at two MODIS bands centered at  $0.65\ \mu\text{m}$  and  $2.11\ \mu\text{m}$  to the cirrus models assumed to be either a single homogeneous layer or three distinct, but contiguous, layers. First, we define the single- and three-layer cirrus cloud models with respect to ice crystal habit and size distribution on the basis of *in situ* replicator data acquired during the First ISCCP Regional Experiment (FIRE-II), held in Kansas during the fall of 1991. Subsequently, fundamental light scattering and radiative transfer theory is employed to determine the single scattering and the bulk radiative properties of the cirrus cloud. Regarding the radiative transfer computations, we present a discrete form of the adding/doubling principle by introducing a direct transmission function, which is computationally straightforward and efficient, an improvement over previous methods.

For the  $0.65\ \mu\text{m}$  band, at which absorption by ice is negligible, there is little difference between the bidirectional reflectances calculated for the one- and three-layer cirrus models, suggesting that the vertical inhomogeneity effect is relatively unimportant. At the  $2.11\ \mu\text{m}$  band, the bidirectional reflectances computed for both optically thin ( $\tau = 1$ ) and thick ( $\tau = 10$ ) cirrus clouds show significant differences between the results for the one- and three-layer models. The reflectances computed for the three-layer cirrus model are substantially larger than those computed for the single-layer cirrus. Finally, we find that cloud reflectance is very sensitive to the optical properties of the small crystals that predominate in the top layer of the three-layer cirrus model. It is critical to define the most realistic geometric shape for the small “quasi-spherical” ice crystals in the top layer for obtaining reliable single-scattering parameters and bulk radiative properties of cirrus.

## 1. Introduction

Cirrus clouds located in the upper troposphere and lower stratosphere are important to the Earth's climate [Liou, 1986; Stephens *et al.*, 1990]. They reflect solar radiation, absorb the thermal emission from ground and lower atmosphere, and reemit infrared radiation to space. The Moderate Resolution Imaging Spectroradiometer (MODIS) [King *et al.*, 1992] on the recently launched Terra spacecraft will enhance the capability for monitoring cirrus clouds in comparison with previous generations of satellite instruments such as the Advanced Very High Resolution Radiometer (AVHRR). MODIS has a total of 36 bands for studies of land, ocean, and the atmosphere, including the 1.38  $\mu\text{m}$  band for cirrus detection and correction [Gao and Kaufman, 1995], 0.65, 1.66, and 2.11  $\mu\text{m}$  bands for implementing cloud microphysical and optical property retrieval techniques [King *et al.*, 1997], and the 8.5, 11, and 12  $\mu\text{m}$  for applying infrared cloud property retrieval techniques [Ackerman *et al.*, 1990]. MODIS data will allow improved retrievals of cirrus optical and microphysical parameters such as optical thickness of cirrus and mean effective size of the ice crystals in these clouds.

Various algorithms have been developed to retrieve cirrus optical and microphysical properties in the past twenty years [e.g., Liou *et al.*, 1990; Ou *et al.*, 1993; Minnis *et al.*, 1993a,b; Rossow and Lacis, 1990]. They can be categorized into the techniques based on either infrared emission or solar reflection. The representative algorithm of the former is the method developed by Inoue [1985] for determining the infrared emissivity of cirrus clouds on the basis of the brightness temperature difference between 11 and 12  $\mu\text{m}$  wavelengths with an assumption of implicit mean particle size. An infrared trispectral algorithm using 8.52, 11, and 12  $\mu\text{m}$  bands [Ackerman *et al.*, 1990, 1998; Strabala *et al.* 1994] with a recent improvement [Baum *et al.* 2000a,b] form the basis of an infrared retrieval algorithm using MODIS infrared channels. The representative retrieval algorithm based on solar reflection is that developed by Nakajima and King [1990], who used a trispectral (0.75, 1.6, and 2.2  $\mu\text{m}$ ) method to simultaneously retrieve the optical thickness and mean effective particle size for

water clouds. This approach has been applied to the retrieval of the optical thickness and mean particle size of ice crystals for cirrus [Wielicki *et al.*, 1990].

To develop a reliable retrieval algorithm for cirrus optical and microphysical properties, it is critical to generate reliable pre-calculated look-up tables of bidirectional reflectance for cirrus clouds over a practical range of effective sizes and optical thicknesses for various solar- and view-angular geometries. At present, most algorithms for retrieving cirrus optical thickness and effective size assume that all ice crystals in cirrus are of one specific habit, such as spheres, hexagonal plates, hexagonal columns, or fractal polycrystals. In addition, it is commonly assumed that a single size distribution is sufficient to determine the scattering properties of the ice crystals within the cirrus layer. However, the observations based on aircraft-borne two-dimensional optical cloud probe (2D-C) and balloon-borne replicator measurements [e.g., Heymsfield and Platt, 1984; Arnott *et al.*, 1994; Mitchell *et al.*, 1996a,b; McFarquhar and Heymsfield, 1996, 1997] have demonstrated that a significant number of ice crystals in cirrus clouds are bullet rosettes, solid and hollow columns, plates, and irregularly shaped aggregates. In addition, Heymsfield and colleagues have showed that ice crystal habits and size distributions are vertically inhomogeneous in cirrus clouds. [<http://box.mmm.ucar.edu/science/cirrus/projects/FIRE>].

Since satellite-based retrieval techniques essentially compare library computations of bidirectional reflectances to actual measurements in their implementations, it is necessary to assess the effect of the inhomogeneity of the ice crystal sizes and shapes within cirrus on the radiative transfer calculations for generating the reflectance libraries. Our objective is to understand the effect of vertical inhomogeneity in the structure of cirrus clouds on their radiative properties. We employ fundamental scattering and radiative transfer theory to investigate the bidirectional reflectance of cirrus clouds at MODIS 0.65 and 2.11  $\mu\text{m}$  bands using *in situ* crystal habit and size distribution for two typical cases of midlatitude cirrus cloud systems.

Section 2 describes the data and models used in this study. In Section 3, we first define three-layer and single homogeneous cirrus models. We then derive the single-scattering properties associated with the two cirrus models. In section 4, we present the differences between bidirectional reflectances computed for the three-layer cirrus model and its one-layer counterpart. Also presented in this section is the sensitivity study regarding the shape effect of the small “quasi-spherically” nonspherical ice crystals on cloud reflectance. Conclusions are given in section 5. Finally, in Appendix we present a numerically stable radiative transfer model based on the adding/doubling principle expressed in a discrete form for calculating reflected and transmitted intensities resulting from multiple scattering and absorption of cirrus clouds.

## **2. Data and Models**

### **a. Data**

The size distributions and ice crystal habit information obtained from two cases of replicator measurements carried out in Kansas during FIRE-II are used in this study. The balloon-borne ice crystal replicators were launched at 1337 UTC on 25 November 1991 and at 2045 UTC on 05 December 1991 and ascended at a rate of  $4 \text{ m s}^{-1}$  while passing through the cloud layers. Cloud top temperature on 25 November was  $-57^{\circ}\text{C}$  and on 5 December was  $-65^{\circ}\text{C}$ , as measured by a radiosonde connected to the balloon package. The replicator collects particles in a liquid plastic solution, which is coated on a moving, 35-mm-wide transparent leader tape. The particles are preserved when the solvent in the solution evaporates, giving detailed ice crystal impressions and size spectra of crystals down to 10 microns and below. The particles do not breakup upon impact on the replicator tape, because of the slow rate of ascent of the balloon. The efficiency with which the replicator collects small crystals has been quantified theoretically and experimentally [Miloshevich and Heymsfield, 1997], and concentrations used in this study are adjusted to account for the non-zero collection efficiencies of small particles. The ice crystals were sized throughout the

depth of the cloud, which, when their concentration was appropriately considered, led to 28 size spectra in the vertical on November 25 and 33 spectra on December 5, each spectra representing approximately 100 m in the vertical.

## b. Single-Scattering Properties

Ice crystal sizes in cirrus clouds fall predominately within the applicable size parameter regime of the geometric optics method at visible and near-infrared wavelengths. Each ray can be localized on the wavefront of incident radiation (electromagnetic wave); consequently, Snell's Law and Fresnel's formulas can be applied to trace the ray propagation and the electric field magnitude as well as polarization configuration associated with the ray. In the conventional geometric optics approach for deriving the scattering properties of a particle, the scattered field in the radiation zone is regarded as the superposition of diffracted rays and Fresnelian rays. The contribution due to ray diffraction can be solved using the standard Fraunhofer theory whereas the contribution of Fresnelian rays can be solved by a ray-tracing calculation. This approach suffers from several shortcomings, as noted by *Yang and Liou* [1995]. In particular, it is assumed that the extinction efficiency is 2 regardless of particle size.

To overcome the shortcomings of the conventional geometric optics, *Yang and Liou* [1996] developed a geometric-optics-integral-equation approach (hereafter referred to as GOM2). According to fundamental electrodynamics theory, the scattered far field can be obtained if the tangential components of the electric and magnetic fields on the particle surface are specified. In principle, GOM2 employs the ray tracing technique to solve the near field on the particle surface and then map the near field to the far field via the following rigorous relationship:

$$\vec{E}^s(\vec{r})|_{kr \rightarrow \infty} = \frac{e^{ikr}}{-ikr} \frac{k^2}{4\pi} \hat{r} \times \oint_S \{ \hat{n}_s \times \vec{E}(\vec{r}') - \hat{r} \times [\hat{n}_s \times \vec{H}(\vec{r}')] \} e^{-ik\hat{r} \cdot \vec{r}'} d^2r', \quad (1)$$

where  $\hat{n}_s$  and  $\hat{r}$  are unit vectors along the normal directions of particle faces and scattering direction, respectively, and  $k = 2\pi/\lambda$  in which  $\lambda$  is the wavelength of incident wave in vacuum. It should be pointed out that the partition of the diffraction and Fresnelian contributions to the far field is not required in GOM2. A simplified algorithm for GOM2 is employed to reduce the computational cost.

To compute the extinction and scattering cross sections of ice crystals, we use the ray tracing technique coupled with the following exact electrodynamic relationships:

$$C_{ext} = \text{Im} \left\{ \frac{k}{|E_o|^2} \iiint_V [\epsilon(\vec{r}') - 1] E(\vec{r}') \cdot E_o^*(\vec{r}') d^3r' \right\}, \quad (2a)$$

$$C_{ab} = \frac{k}{|E_o|^2} \iiint_V \epsilon_i(\vec{r}') E(\vec{r}') \cdot E^*(\vec{r}') d^3r', \quad (2b)$$

where  $\vec{E}_o$  is the electric field associated with incident wave,  $\epsilon = \epsilon_r + i\epsilon_i$  is the complex permittivity, and the asterisk indicates the complex conjugate operation. The volume integrals in Eqs.(2a) and (2b) are carried out along individual ray paths inside the particle via a Monte Carlo/ray-by-ray algorithm [Yang and Liou, 1997] that is a generalization of the well-known anomalous diffraction theory [van de Hulst, 1957].

Because of the complicated mechanisms involved in ice crystal growth, such as sublimation, riming or aggregation of particles observed in anvils, the surfaces of ice crystals may be rough. Roughened ice crystal surfaces were observed in laboratory experiments [Cross, 1968] and also verified by recent *in situ* observations of tropic anvil cirrus clouds [Heymsfield *et al.*, to be available at <http://box.mmm.ucar.edu/science/cirrus>]. The scattering phase functions of roughened particles display less variation [Macke *et al.*, 1996; Yang and Liou, 1998] than their counterparts for ice crystals containing smooth facets. As articulated by Mishchenko *et al.* [1996] on the basis of ground-based nephelometer and aircraft radiance measurement of cirrus clouds [Foot, 1988; Francis,

1995; Gayet, 1995; Posse and von Hoyningen-Huene 1995], the scattering phase functions of cirrus clouds can be rather featureless with no appreciable halos.

Based on these studies, we account for surface roughness specifically for ice crystal aggregates in this study. In the numerical computation, the particle surface is regarded as a number of small facets whose normal direction is tilted from that in the smooth case, specified by local zenith and azimuth angles  $\theta$  and  $\varphi$ . The slope of a facet along two orthogonal directions that are perpendicular to the local zenith direction, say  $x$  and  $y$  directions, can be specified by

$$Z_x = \frac{\partial Z}{\partial x} = (\mu^{-2} - 1)^{1/2} \cos \varphi, \quad (3a)$$

$$Z_y = \frac{\partial Z}{\partial y} = (\mu^{-2} - 1)^{1/2} \sin \varphi, \quad (3b)$$

where  $\mu = \cos \theta$ . The derivatives in Eqs.(3a) and (3b) are confined to the facet. Since there is no sufficient quantitative experimental information on the roughness of ice crystal surfaces at present, we assume that irregular roughness of ice crystal surfaces is similar to that of a wavy sea surface, which can be specified by the Gram-Charlie distribution [Cox and Munk, 1954]. If the tilt distribution of the roughness is azimuthally homogeneous (i.e., independent of angle  $\varphi$ ), the statistical probability density function for the condition that the slopes of a facet along the two axis directions are given by the first order Gram-Charlie, or a 2-D Gaussian distribution, as follows:

$$P(Z_x, Z_y) = \frac{1}{\pi \sigma^2} \exp[-(Z_x^2 + Z_y^2)/\sigma^2], \quad (4)$$

where  $\sigma$  is a parameter determining the magnitude of roughness. It is noted that  $\sigma=0-0.005$ ,  $0.005-0.05$ ,  $0.05-0.3$  correspond to slight, moderate, and deep roughness in the single-scattering calculation, respectively. The technical details in accounting for the surface roughness in the light scattering computation on the basis of geometric optics method have been presented by Yang and Liou [1998].

### **c. Radiative Transfer Model**

Radiative transfer calculations for cirrus are performed using the adding/doubling method. The adding/doubling principle has been expressed mathematically in a matrix form [Twomey, 1966; Hunt and Grant, 1966] and in an integral form [Hansen and Travis, 1974]. A concise formulation in a discrete form for the adding/doubling method is provided in Appendix, where we also address some numerical concerns in the radiative transfer computation such as the truncation of forward peak of the phase function and a stable expansion of the phase function in terms of the re-normalized Legendre function. The discrete expression of the adding/doubling principle is straightforward and efficient in numerical realization. The present adding/doubling computational program has been validated with respect to the various cases presented by Lenoble [1985] and also in comparison with DISORT [Stamnes *et al.*, 1988, 2000] for a number of canonical problems.

## **3. Development of Cirrus Models**

### **a. The Cirrus 3-Layer Model**

The vertically inhomogeneous nature of cirrus clouds was observed during the FIRE-II program. Figures 1a and 1b show two different vertical profiles based on replicator images of ice crystals in cirrus clouds collected on November 25 and December 5, 1991 [Heymsfield *et al.* <http://box.mmm.ucar.edu/science/cirrus>]. Three distinct regimes of ice crystals are evident from the replicator data. In the uppermost layer, small nonspherical “quasi-spheres” are predominant. These particles are essentially nonspherical shapes with an aspect ratio approaching 1. The term “quasi-spherical” used in the analysis of observed data and in many theoretical studies is often misleading because the optical properties of spherical and nonspherical particles are significantly different even if the nonsphericity of particle geometry is not substantial. The middle layer of cirrus is primarily composed of pristine ice crystals with well-defined hexagonal shapes or bullet rosettes. The bottom layer

contains larger but irregular ice crystals. Roughness can also be noted from the replicator images of the irregular ice crystals. In both images, it becomes apparent that the particles increase in size and the shapes become more complex from the top to the base of the cirrus.

The dominant habits of ice crystals and size distributions have been observed with a fine vertical-resolution for the two cases shown in Fig.1a and 1b (28 and 33 layer data were obtained in FIRE-II *in situ* observations for the November 25 and December 5 cases, respectively). Based on these data, we constructed the percentages of the various ice crystal habits and size distributions for the top, middle, and bottom layers of cirrus clouds. For a given layer centered at  $z$  with thickness of  $\Delta z$ , the mean size distribution and percentage of a specific habit are given by

$$\bar{n}(D, z) = \frac{1}{\Delta z} \int_{z-\Delta z/2}^{z+\Delta z/2} n(D, z') dz', \quad (5a)$$

$$\bar{f}_i(D, z) = \frac{\int_{z-\Delta z/2}^{z+\Delta z/2} f_i(D, z') n(D, z') dz'}{\int_{z-\Delta z/2}^{z+\Delta z/2} n(D, z') dz'}, \quad (5b)$$

where  $D$  is the maximum dimension of ice crystals. The preceding averaging procedure is also applied to obtain the mean size distribution and habit percentage for cirrus by assuming a single size distribution to represent the cirrus cloud.

To illustrate the differences between the use of a 3-layer model and a single-layer cirrus model, we first confine our discussion to the November 25 case. The thicknesses of the top, middle, and bottom layers are 0.79, 0.73, and 1.18 km, respectively. The size distributions and crystal habit percentages for the three layers are shown in panels A-C of Fig.2a. For the uppermost cirrus layer, “quasi-spherical” habits are dominant for the small particle mode ( $D < 100 \mu\text{m}$ ), whereas bullet rosettes are dominant for the large particle mode ( $D > 100 \mu\text{m}$ ). The middle layer is composed primarily of columns and bullets. In the bottom layer, ice crystals are mainly irregular aggregates, but the edges seem to be rounded, perhaps

due to the effects of sublimation. The percentages of various ice crystal habits for the entire cirrus layer with a thickness of 2.7 km are shown in the panel D of Fig.2a. It can be noted that two geometries (sphere and hexagon) are used for the small ice crystals, as illustrated in panels A and D of Fig.2a. The two particle morphologies are used for understanding the sensitivity of the radiative properties of cirrus to these small ice crystals, which is of concern in remote sensing and radiative transfer modeling. This is because these small ice crystals are often misidentified as spheres in observations based on the particle images with blurred edges. Even using an optical microscope, the shapes of small ice crystals are unlikely to be seen clearly because of the poor instrumental resolving power caused by optical diffraction phenomenon [Ohtake, 1970].

Shown in Fig2b are the size distributions and habit percentages for the case of December 5. The thicknesses of the three layers (1.24, 1.12, and 1.17 km) in this case are more uniform in comparison with the case of November 25. In addition, the former is thicker. The December 5 case had a much colder cloud top and the crystal population was more pristine, in that many columns and few polycrystals (rosettes) were observed. The division of large and small modes for ice crystal habits is at 50  $\mu\text{m}$  for the case of December 5. It can be noted that for the small mode, “quasi-spherical” ice crystals are dominant. There are substantially large numbers of “quasi-spherical” particles even for the middle layer. According to Figs.2a and 2b, both size distributions and ice crystal habits vary substantially with altitude. It should be pointed out that a three-layer or multiple-layer cirrus model is realistic as a general rule, as is evident from replicator data shown and also from the composite cirrus morphology based on radar observation [Mace *et al.*, 1997]. In the following discussions, we select the December 5 case to investigate the effect of vertical inhomogeneity on single- and multiple-scattering properties of cirrus.

## **b. Radiative properties of cirrus layers**

We employ the scattering computational model described in Section 2 to compute the extinction cross sections, single-scattering albedos, and phase functions for ice crystals.

Ice crystals are assumed to be orientated randomly in the atmosphere. First, to characterize the bulk properties of size distribution, we define the mean maximum dimension for a given size distribution as follows:

$$\langle D \rangle = \frac{\int_{D_{\min}}^{D_{\max}} Dn(D)dD}{\int_{D_{\min}}^{D_{\max}} n(D)dD}, \quad (6)$$

where  $D_{\min}$  and  $D_{\max}$  are the cutoffs of size distribution at small and large sizes, respectively. *Foot* [1988], *Francis et al.* [1994], *Fu* [1996], and *Wyser and Yang* [1998] have found that with this definition for mean particle size, the details of the size distribution are not important in specifying the bulk optical properties of cirrus. This feature has also been observed in the case of water clouds composed of liquid droplets whose scattering properties can be solved using Mie theory [*Hansen and Travis*, 1974; *Hu and Stamnes*, 1993]. Following these studies, we define the effective diameter  $D_e$  and effective radius  $r_e$  for nonspherical ice crystals with a combination of various habits as follows:

$$D_e = 2r_e = \frac{3 \int_{D_{\min}}^{D_{\max}} \sum_i V_i(D) f_i(D) n(D) dD}{2 \int_{D_{\min}}^{D_{\max}} \sum_i A_i(D) f_i(D) n(D) dD}, \quad (7)$$

where  $f_i(D)$  is the percentage of a specific habit at size  $D$ . The summation is carried out for all the ice crystal habits. We note that the preceding definition of effective radius reduces to that defined by *Hansen and Travis* [1974] in the case of spherical particles, i.e.,  $r_e = \langle r^3 \rangle / \langle r^2 \rangle$ . The mean extinction cross section, single-scattering albedo, and phase function are given by

$$\bar{\sigma}_e = \frac{\int_{D_{\min}}^{D_{\max}} \sum_i \sigma_e(D) P(\Theta, D) f_i(D) n(D) dD}{\int_{D_{\min}}^{D_{\max}} \sum_i f_i(D) n(D) dD}, \quad (8a)$$

$$\bar{\omega} = \frac{\int_{D_{\min}}^{D_{\max}} \sum_i \sigma_s(D) P(\Theta, D) f_i(D) n(D) dD}{\int_{D_{\min}}^{D_{\max}} \sum_i \sigma_e(D) f_i(D) n(D) dD}, \quad (8b)$$

$$\bar{P}(\Theta) = \frac{\int_{D_{\min}}^{D_{\max}} \sum_i \sigma_s(D) P(\Theta, D) f_i(D) n(D) dD}{\int_{D_{\min}}^{D_{\max}} \sum_i \sigma_s(D) f_i(D) n(D) dD}. \quad (8c)$$

Figure 3 shows the bulk microphysical and optical properties for the size distributions measured for the December 5 case. The upper row shows the geometric configuration of the three layers of cirrus and the mean maximum dimension and effective size of ice crystals in these layers. The second and third rows show the extinction coefficient and single-scattering albedo. The lower two rows provide the asymmetry parameter of the phase functions and the fraction of delta transmission [Takano and Liou, 1989a] in scattered energy. Note that the delta-transmission is an artifact pertaining to the ray-tracing technique, which can be circumvented by using a more accurate physical optics approach [Mishchenko and Macke, 1998]. In the present GOM2 calculation based on a simplified algorithm [Yang and Liou, 1996], we do not account for the spreading of the rays associated with delta-transmission for size parameter larger than 100. The use of either a geometric optics method or a physical optics approach in dealing with delta transmission in the single-scattering calculation for large size parameters does not make a significant difference in the radiative transfer computation. The mean maximum dimension of the ice crystals is 30  $\mu\text{m}$ , 80  $\mu\text{m}$ , and 132  $\mu\text{m}$  for the top, middle, and lower cirrus layers, respectively. The mean effective diameters are 47, 92, and 89  $\mu\text{m}$  for the top, middle, and bottom layers, respectively. The bottom layer has a smaller ratio of volume to projected area

in comparison with the middle layer because of the porous structures of ice crystal aggregates.

The optical properties of ice crystals are computed at two MODIS bands centered at 0.65 and 2.11  $\mu\text{m}$ . In the computation, the MODIS instrumental response functions at these channels have been accounted for. At MODIS 0.65 and 2.11  $\mu\text{m}$  bands, the maximum extinction coefficient occurs in the middle layer because the number concentration of ice crystals is highest for this layer. At the 2.11  $\mu\text{m}$  band, the single-scattering albedo is higher in the top layer than in the lower layers due to the prevalence of small crystals. At both two bands, the asymmetry parameter is smaller in the top and bottom layers than in the middle layer. In the top layer, the asymmetry parameter is reduced because the particles are smaller and the forward peak of the phase function is weaker, while in the bottom layer, the reduced asymmetry parameter is caused by the particle roughness. The vertical variability of delta transmission is similar to that of the asymmetry parameter. In the top layer, delta-transmission is substantially reduced due to the ray-spreading effect associated with small size parameters [Yang and Liou, 1996]. In the bottom layer, the roughness of particle surface also reduces the delta-transmission effect.

Figure 4 shows the phase functions associated with the single-scattering properties shown in Fig. 3. At the 0.65  $\mu\text{m}$  band, substantial differences between the phase functions for the bottom layer and other layers can be noted at scattering angles near  $120^\circ$ . The phase function values for the bottom layer are much larger than those for the top and middle layers in the scattering region between  $5^\circ$  and  $20^\circ$ . Evidently, the phase function values computed by assuming that cirrus are homogeneous are significantly different from the phase functions of the three layers in some specific scattering regions. At the 2.11  $\mu\text{m}$  band, the forward peaks of the phase functions are smaller than at the 0.65  $\mu\text{m}$  band because the size parameters are smaller. It can also be noted that the magnitude of the phase function in the side scattering and backscattering regions are much lower at the 2.11  $\mu\text{m}$  band than at 0.65

$\mu\text{m}$  band. In addition, the differences of the phase functions for different layers are enhanced at the  $2.11 \mu\text{m}$  band because the particle absorption is strongly sensitive to the particle sizes.

## 4. Results

### A. Comparison of reflectance feature for two cirrus models

We use the radiative transfer model described in Appendix to compute the bi-directional reflectance to compare the radiative features of the three-layer and single-layer cirrus models. To understand the physics in the comparison, one needs to interpret the scattering geometry involving the sun and a satellite. For a given solar geometry specified by  $(\theta_s, \varphi_s)$  and view geometry specified by  $(\theta_v, \varphi_v)$ , the corresponding scattering angle is given by

$$\Theta = \cos^{-1}[-\cos\theta_s \cos\theta_v + \sin\theta_s \sin\theta_v \cos\phi], \quad (9)$$

where  $\phi = \varphi_s - \varphi_v$  is the relative azimuth angle between sun and satellite. Note that  $\theta_s$  and  $\theta_v$  are the inclination angles measured from zenith. Figure 5 illustrates the contours of scattering angles versus solar- and view-zenith angles for four cases of azimuth angles. The solar zenith and viewing zenith angles range between  $0^\circ$  and  $60^\circ$ . It can be seen that the scattering angles for the region of view-solar geometry considered in the present study are essentially for side scattering and backscattering directions. The variational pattern of the scattering angle versus solar-zenith and viewing-zenith angles depends on the relative azimuth angle. A similar contour diagram of the scattering angle versus  $\cos(\theta_s)$  and  $\cos(\theta_v)$  has been presented by *Mishchenko et al.* [1996].

Figure 6 shows the relative difference between the computed bidirectional reflectances of the three-layer and one-layer cirrus models for optically thin cirrus ( $\tau = 1$ ) at  $0.65 \mu\text{m}$ . The relative difference is defined as

$$e(\theta_s, \theta_v, \phi) = 100[R_3(\theta_s, \theta_v, \phi) - R_1(\theta_s, \theta_v, \phi)] / R_1(\theta_s, \theta_v, \phi), \quad (10)$$

where  $R_3$  and  $R_1$  are the bidirectional reflection functions computed using the three-layer and one-layer cirrus models, respectively. The maximum difference in this case is about 5%. When the optical thickness is small, the photons originating from single scattering events dominate the total radiance. The contribution of single-scattering events to the radiance in the three-layer case is given by

$$r(\theta_s, \theta_v, \phi) = \frac{1}{4 \cos \theta_s \cos \theta_v} \sum_{l=1}^3 [\tilde{\omega}_l \Delta \tau_l P_l(\theta_s, \theta_v, \phi)], \quad (11)$$

where the summation is carried for all three layers of cirrus. Thus, for thin cirrus the bidirectional reflectance function is linearly proportional to the phase function. Referring to Figs. 3 and 5, the contours shown in Fig.6 can be explained as follows. For azimuth angles of  $0^\circ$  and  $60^\circ$ , the maximum difference is observed near scattering angles of  $120^\circ$ , which corresponds to the phase function difference at these scattering angles. For azimuth angles of  $120^\circ$  and  $180^\circ$ , the maximum difference for the three-layer and one-layer results are mainly noted near scattering angles of  $155^\circ$  and  $180^\circ$ .

Figure 7 is similar to Fig.6, except that the optical thickness of the cloud is 10. The contribution of multiple scattering increases with increasing optical thickness. The differences occur at scattering angles between  $90^\circ$  and  $120^\circ$ , between  $150^\circ$  and  $160^\circ$ , and between  $170^\circ$ - $180^\circ$ . From Figs. 6 and 7, the difference between the three-layer and one-layer models is within a few percent regardless of optical thickness. Based on these results, modeling the cirrus as a single layer would seem to be sufficient at visible wavelengths.

Figures 8 and 9 are similar to Figs. 6 and 7, except that the calculations are performed at the  $2.11 \mu\text{m}$  band. Absorption by ice at the  $2.11 \mu\text{m}$  band is much higher than at the  $0.65 \mu\text{m}$  band. It is noted that the reflectance for the three-layer model is always larger than the one-layer model at the  $2.11 \mu\text{m}$  band. With the absorption of ice at the  $2.11$

$\mu\text{m}$  band, the top layer of cirrus dominates the contribution to the cloud reflectance because photons that penetrate into the lower layers are largely absorbed. The mean size of the ice crystals in the top layer is much smaller than that associated with the general one-layer cirrus model. With the increase of optical thickness, the difference between the three-layer and one-layer models increases. For an optical thickness of 10, the differences can reach up to 50%. Because the 2.11  $\mu\text{m}$  band is used for the retrieval of the mean size and optical depth of cirrus cloud, it is expected that the vertical inhomogeneity may be important to developing more realistic cirrus retrieval algorithms. In comparing Figs. 8 and 9, it may be noted that the difference between the three-layer and one-layer models depends mainly on the scattering angle when the cloud is optically thin. However, for optically thick cirrus, the difference depends not only on scattering angle but also strongly on the viewing zenith and solar zenith angles. This is because the radiance path varies with the solar and view angles. For large solar zenith or viewing zenith angles, the ray path is large and the difference between the three-layer and one-layer cirrus models, and their associated single-scattering properties, becomes more significant.

#### **B. Sensitivity of cirrus reflectance to shapes of “quasi-spherical” particles**

As discussed in Section 3a regarding the replicator images of ice crystals, the small so-called “quasi-spherical” ice crystals are essentially not spherical. Whether their morphologies can be treated as spheres in light scattering and radiative transfer calculations depends on the wavelength of radiation. At a far infrared wavelength, say, 15  $\mu\text{m}$  or larger, the nonsphericity of these particles may not be significant in comparison with wavelength because the size parameter becomes small. In this case, spherical and spheroidal geometries have been used in light scattering computations [e.g., *Sun and Shine*, 1994; *Takano et al.*, 1992]. However, for the 0.65 and 2.11  $\mu\text{m}$  bands, the size parameter for a small particle, say on the order of 20  $\mu\text{m}$ , is approximately 100 and 30 at the band centers, respectively. For a size parameter on these orders, the nonsphericity effect of a particle on its scattering properties can be significant.

To investigate the sensitivity of cirrus optical properties to the shapes assumed for the small “quasi-spherical” ice crystals, in this study we compare the results associated with spherical and hexagonal (with an aspect ratio of unity) assumption for the morphologies of these particles. The “quasi-spherical” particles primarily affect the top and middle layers and are largely absent in the bottom layer. The effective sizes for the top and middle layers are 47.5  $\mu\text{m}$  and 93.0  $\mu\text{m}$  if hexagonal shapes are used for the “quasi-spherical” particles whereas the sizes are 52.2  $\mu\text{m}$  and 94.6  $\mu\text{m}$  if perfect spherical geometry is assumed for these particles. Evidently, the assumption of shape for the “quasi-spherical” ice crystals in cirrus clouds can lead to a change of effective size by as much as 5  $\mu\text{m}$ .

Table 1 lists the single-scattering properties of the top and middle layers. Substantial differences are noted for delta transmissions at MODIS 0.65  $\mu\text{m}$  band because of the absence of parallel faces in spheres. The asymmetry factor of the phase function is substantially different at the 2.11  $\mu\text{m}$  band, showing the dependence of the scattering properties on the assumption of habits. The differences of the results for the two shapes are larger for the top layer than for the middle layer because the former has a larger population of “quasi-spherical” ice crystals.

Figure 10 shows the phase functions associated with the single-scattering properties listed in Table 1. Substantial differences of the phase functions can be seen for the top layer at both the 0.65 and 2.11  $\mu\text{m}$  bands. The overall feature is that the spherical assumption leads to larger phase function values for scattering angles between  $10^\circ$  and  $45^\circ$  and lower values at side scattering angles. However, the spherical assumption leads to a pronounced scattering maximum between  $130^\circ$  and  $140^\circ$ , which corresponds to the rainbow feature of ice spheres. Additionally, the spherical assumption leads to larger phase function values near  $180^\circ$  (backscattering) at the 2.11  $\mu\text{m}$  band. In the middle layer, the differences caused by the assumption of habit for the small particles are reduced due to the small number of the

small particles in the size distribution. Evidently, using the most realistic particle shapes for the small particles in the top layer of cirrus will be crucial to obtaining reliable single-scattering properties of the cloud.

Shown in Figs. 11 and 12 are the difference of bidirectional reflectances computed using nonspherical hexagonal and spherical geometries in the three-layer for thin ( $\tau=1$ ) and thick ( $\tau=10$ ) cirrus at the 2.11  $\mu\text{m}$  band. The differences shown in Figs. 11 and 12 are defined as

$$e(\theta_s, \theta_v, \phi) = 100[R_{\text{sph}}(\theta_s, \theta_v, \phi) - R_{\text{hex}}(\theta_s, \theta_v, \phi)] / R_{\text{hex}}(\theta_s, \theta_v, \phi), \quad (12)$$

where  $R_{\text{sph}}$  and  $R_{\text{hex}}$  indicate the reflection functions associated with spherical and hexagonal shapes, respectively, which are assumed for the small “quasi-spherical” ice crystals. The maximum differences shown in Fig. 11, which correspond to scattering angles between  $130^\circ$  and  $140^\circ$ , are caused by the rainbow feature of ice spheres. It can also be noted that the assumption of ice spheres leads to an overestimation of reflectance near  $180^\circ$  (backscattering). As optical thickness increases, the contrast decreases for the rainbow feature. However, the enhanced backscattering for the assumption of spheres is still noticeable. For optically thick cirrus, Fig. 12 shows that the assumption of sphere for the “quasi-spherical” particles leads to an underestimation of cloud reflection at the 2.11  $\mu\text{m}$  band except for scattering angles near  $180^\circ$ .

Figures 13 and 14 are similar to Figs. 11 and 12, except that the formers are for the 0.65  $\mu\text{m}$  band. Again, we see pronounced differences between the results associated with the hexagonal and spherical assumptions for the small ice crystals in the uppermost layer. The positive maximum near the backscattering peak noted in Figure 11, however, is not observed in the results shown in Figure 13 because the phase function value for the spheres is less than that of the hexagons at the 0.65  $\mu\text{m}$  band. Additionally at the 0.65  $\mu\text{m}$  band, a distinct rainbow feature can be noted in the case of thin cirrus. For the optically thick cirrus, the rainbow is blurred due to multiple scattering events occurring within the clouds. Figures

11 through 14 illustrate that the shape effect of the small ice crystals at the top layer of cirrus is significant at both visible and near infrared wavelengths.

## 5. Conclusions

In this study, we have defined a three-layer cirrus model in terms of ice crystal habit and size distribution based on *in-situ* replicator data acquired during the NASA FIRE-II field observation program. We have described a fundamental scattering model and a numerically stable radiative transfer model for the computation of the single-scattering properties of various ice crystals and the bidirectional reflection of cirrus clouds.

We have found that the effect of vertically inhomogeneity within cirrus is not significant at MODIS 0.65  $\mu\text{m}$  band, a wavelength for which the absorption of ice is negligible. However, in comparison with the one-layer cirrus model, a vertically inhomogeneous cirrus cloud produces substantially larger reflectance at the 2.11  $\mu\text{m}$  band, a wavelength for which absorption by ice is important. The increase in reflectance occurs because the mean size of ice crystals in the top layer in the three-layer model is smaller than in the case of the one-layer model and the total reflected radiance is dominated by the contribution from the top layer. For a given optical thickness, the reflectance increases with decreasing particle size.

We also investigated the sensitivity of reflection of cirrus clouds to the particle shapes of the “quasi-spherical” ice crystals that have been often assumed to be spheres. Numerical results have demonstrated that the bidirectional reflection function of cirrus is very sensitive to the shape of these particles at both visible and near-infrared wavelengths.

## Appendix : A Discrete Expression of Adding/Doubling Principle

The adding/doubling method is one of most robust approaches to solve the radiative transfer equation for multiple scattering events. The standard mathematical expression of this method involves various tedious angular integrals although it can be written symbolically in a very simple form. In this section we present a discrete form of the method by introducing a direct transmitting function. As an improvement over previous mathematical expressions from a practical viewpoint, the discrete adding/doubling equations are straightforward and more efficient in numerical implementation. In addition, the discrete form of the adding/doubling method is more suitable for addressing some numerical concerns, such as the numerical singularity of adding/doubling calculation and the performances of various quadrature schemes.

To economize computational cost and memory requirements, we apply a Fourier expansion over the azimuth angle for radiance and bidirectional reflection and transmission functions:

$$I^{i,r,t}(\mp\mu, \varphi) = \sum_{m=0}^M I^{i,r,t(m)}(\mp\mu) \cos m\varphi, \quad (\text{A1a})$$

$$r(\mu, \varphi, \mu', \varphi') = \sum_{m=0}^M r^{(m)}(\mu, \mu') \cos m(\varphi - \varphi'), \quad (\text{A1b})$$

$$t(\mu, \varphi, \mu', \varphi') = \sum_{m=0}^M t^{(m)}(\mu, \mu') \cos m(\varphi - \varphi'). \quad (\text{A1c})$$

where superscripts i, r, and t indicate incident, reflected, and transmitted intensities, respectively; and  $\mu$  and  $\mu'$  are positive with allowable values in  $[0,1]$ . The maximum number of Fourier terms ( $M$ ) required for the convergent solutions of Eqs.(A1a)-(A1c) depends on the incoming and outgoing radiation beams as well as the magnitude of the asymmetry of the phase function. For example, only the first term is necessary for a solar zenith angle of  $0^\circ$  (overhead Sun) whereas more than 100 terms may be required for a low solar elevation angle (Sun near the horizon). For solar zenith and viewing zenith angles

smaller than  $60^\circ$ , 30 to 40 terms are normally required in the case of cirrus clouds if the strong forward peak of the phase function is truncated. A comprehensive study regarding the number of the terms required in the Fourier series has been carried out by *King* [1983] using Henyey-Greenstein function and the phase function for a fair weather cumulus.

According to the definitions of reflection and transmission functions [*Hansen and Travis*, 1974], it can be proven that the Fourier components of reflected and transmitted intensities are given by

$$I^{r(m)}(\mu) = (1 + \delta_{m0}) \int_0^1 r^{(m)}(\mu, \mu') I^{i(m)}(-\mu') \mu' d\mu', \quad (\text{A2a})$$

$$I^{t(m)}(\mu) = (1 + \delta_{m0}) \int_0^1 t^{(m)}(\mu, \mu') I^{i(m)}(-\mu') \mu' d\mu', \quad (\text{A2b})$$

where  $\delta_{m0}$  is Kronecker delta function. It should be pointed out that the radiances defined in Eqs.(A2a) and (A2b) are diffusive intensities, i.e., they originate from the scattering of incident radiation by the particles in the scattering layer. If the total (direct + diffuse) transmitted intensity, indicated as  $\tilde{I}^t(-\mu, \varphi)$ , is defined in the same manner as in the diffusive case, it follows that

$$\begin{aligned} \tilde{I}^{t(m)}(\mu) &= (1 + \delta_{m0}) \int_0^1 \tilde{t}^{(m)}(\mu, \mu') I^{i(m)}(-\mu') \mu' d\mu' \\ &= (1 + \delta_{m0}) \int_0^1 [t^{(m)}(\mu, \mu') + \Delta^{(m)}(\mu, \mu')] I^{i(m)}(-\mu') \mu' d\mu', \end{aligned} \quad (\text{A3a})$$

where  $\tilde{t}^{(m)}(\mu, \mu')$  is the  $m$ th Fourier component of the total transmission function.

$\Delta^{(m)}(\mu, \mu')$  is associated with the transmission of incident radiation and given by

$$\Delta^{(m)}(\mu, \mu') = \frac{1}{(1 + \delta_{m0})\mu'} \exp(-\tau/\mu') \delta(\mu - \mu'), \quad (\text{A3b})$$

in which  $\delta(\mu - \mu')$  is the Dirac delta function. Evidently, the quantities defined in Eqs.(A2a)-(A3b) are continuous functions of the arguments  $\mu$  and  $\mu'$  that range

continuously in the interval  $[0,1]$ . We select a set of discrete points in the region  $[0,1]$  for  $\mu$  and  $\mu'$ , that is, the two variables can only have the values of  $[\mu_1, \mu_2, \dots, \mu_n]$ . With respect to the discrete set, we define the following discrete quantities with single subscript and double subscripts:

$$I_j^{i,t(m)} = I^{i,t(m)}(-\mu_j), \quad I_j^{r(m)} = I^{r(m)}(\mu_j), \quad (\text{A4a})$$

$$r_{kj}^{(m)} = r^{(m)}(\mu_j, \mu_k), \quad t_{kj}^{(m)} = t^{(m)}(\mu_j, \mu_k) \quad (\text{A4b})$$

$$\tilde{t}_{kj}^{(m)} = \tilde{t}^{(m)}(\mu_j, \mu_k), \quad \Delta_{kj}^{(m)} = \Delta^{(m)}(\mu_j, \mu_k). \quad (\text{A4c})$$

Since the continuous region  $[0,1]$  is discretized by using a set of points, it is required that an integration of a function  $f(\mu)$  with respect to its argument defined in  $[0,1]$  be replaced by a discrete summation in the form of

$$\int_0^1 f(\mu) d\mu \rightarrow \sum_{i=1}^n f(\mu_i) W_i, \quad (\text{A5})$$

where  $W_i$  are the weights in the summation. For an integral involving the Dirac delta function, the definition of the delta function and Eq.(A5) lead to the following relationship:

$$f(\mu_i) = \int_0^1 f(\mu) \delta(\mu - \mu_i) d\mu \rightarrow \sum_{j=1}^n f(\mu_j) W_j \delta(\mu_j - \mu_i). \quad (\text{A6})$$

Evidently, to guarantee the equality in Eq.(A6) in the discrete procedure, the Dirac delta function should be replaced by Kronecker symbol in the form of

$$\delta(\mu_j - \mu_i) \rightarrow \delta_{ji} / W_j = \begin{cases} 1/W_j & \text{for } j = i \\ 0 & \text{for } j \neq i \end{cases}. \quad (\text{A7})$$

Thus, the direct transmission function in discrete form is given by

$$\Delta_{ij}^{(m)}(\tau) = \frac{1}{(1 + \delta_{m0}) W_j \mu_j} \exp(-\tau / \mu_j) \delta_{ij}. \quad (\text{A8})$$

For the discrete quantities defined with respect to the set of discrete points  $[\mu_1, \mu_2, \dots, \mu_n]$ , we introduce a mathematical operator  $\otimes$  defined by

$$A_{ij}^{(m)} \otimes B_{jk}^{(m)} = (1 + \delta_{m0}) \sum_{j=1}^n A_{ij}^{(m)} B_{jk}^{(m)} \mu_j W_j, \quad (\text{A9a})$$

$$C_j^{(m)} \otimes B_{jk}^{(m)} = (1 + \delta_{m0}) \sum_{j=1}^n C_j^{(m)} B_{jk}^{(m)} \mu_j W_j. \quad (\text{A9b})$$

The operator  $\otimes$  is similar to an ordinary matrix multiplication except that a weight is included in the former. Thus, for one homogeneous layer, the reflected, diffusely transmitted, and total transmitted radiances are related to the incident radiation via the following relationships:

$$I_k^{r(m)} = I_j^{i(m)} \otimes r_{jk}^{(m)}, \quad I_k^{t(m)} = I_j^{i(m)} \otimes t_{jk}^{(m)}, \quad \tilde{I}_k^{t(m)} = I_j^{i(m)} \otimes \tilde{t}_{jk}^{(m)}. \quad (\text{A10})$$

One of the interesting features of using the operator  $\otimes$  is the variation of subscripts in the expressions in Eq.(A10): the incident beam denoted by subscript  $j$  is re-directed to the direction denoted by subscript  $k$  after interacting with the scattering layer. Similarly, for two layers indicated by superscripts  $a$  and  $b$ , we have the following relationships:

$$I_k^{r(m)} = I_j^{i(m)} \otimes [r_{jk}^{a(m)} + \tilde{t}_{jl}^{a(m)} \otimes U_{ln}^{(m)} \otimes \tilde{t}_{nk}^{a*(m)}], \quad (\text{A11a})$$

and

$$\tilde{I}_k^{t(m)} = I_j^{i(m)} \otimes [\tilde{t}_{jl}^{a(m)} \otimes \tilde{t}_{lk}^{b(m)} + \tilde{t}_{jl}^{a(m)} \otimes D_{ln}^{(m)} \otimes \tilde{t}_{nk}^{b(m)}], \quad (\text{A11b})$$

where the asterisk indicates that the transmission function corresponds to the case of illumination coming from below. The quantities  $D$  and  $U$  in Eqs.(A11a) and (A11b) are given by

$$D_{ij}^{(m)} = \sum_{n=1}^N D_{ij}^{(m),(n)}, \quad U_{ij}^{(m)} = r_{ij}^{b(m)} + D_{il}^{(m)} \otimes r_{lj}^{b(m)}, \quad (\text{A12a})$$

$$D_{ij}^{(m),(n+1)} = D_{il}^{(m),(n)} \otimes D_{lj}^{(m),(1)}, \quad D_{ij}^{(m),(1)} = r_{il}^{b(m)} \otimes r_{lj}^{a*(m)}. \quad (\text{A12b})$$

According to the sensitivity study by *Hansen and Travis* [1974], we use  $N=12, 5$ , and  $3$  in the summation involved in the first expression in Eq.(A13a) for  $m<10$ ,  $10<m<100$ , and  $m>100$ , respectively. The remaining terms are approximated by a geometric series. The physics of the adding/doubling principle can be viewed clearly in terms of the variations of the subscripts from left to right in the right-hand sides of Eqs.(A11a) and (A11b). The reflection and transmission functions for the combined layer are given by

$$R_{jk}^{(m)} = r_{jk}^{a(m)} + \tilde{t}_{jl}^{a(m)} \otimes U_{ln}^{(m)} \otimes \tilde{t}_{nk}^{a*(m)}, \quad (\text{A13a})$$

and

$$\tilde{T}_{jk}^{(m)} = \tilde{t}_{jl}^{a(m)} \otimes \tilde{t}_{lk}^{b(m)} + \tilde{t}_{jl}^{a(m)} \otimes D_{ln}^{(m)} \otimes \tilde{t}_{nk}^{b(m)}. \quad (\text{A13b})$$

The transmission function given in Eq. (A13b) contains the contribution due to direct transmission, which is implicitly in the form of a delta function, and it may potentially cause inaccuracy in numerical computation. Thus, it is necessary to separate the diffusive and direct components in Eq.(A13b). It is noted that

$$\begin{aligned} \tilde{t}_{jl}^{a(m)} \otimes \tilde{t}_{lk}^{b(m)} &= [t_{jl}^{a(m)} + \Delta_{jl}^{(m)}(\tau_a)] \otimes [t_{lk}^{b(m)} + \Delta_{lk}^{(m)}(\tau_b)] = \\ &= t_{jl}^{a(m)} \otimes t_{lk}^{b(m)} + \exp(-\tau_a / \mu_j) t_{jk}^{b(m)} + t_{jk}^{a(m)} \exp(-\tau_b / \mu_k) + \Delta_{jk}^{(m)}(\tau_a + \tau_b). \end{aligned} \quad (\text{A14})$$

Thus, the diffusive transmission function for the combined layer is given by

$$\begin{aligned} T_{jk}^{(m)} &= t_{jl}^{a(m)} \otimes t_{lk}^{b(m)} \\ &+ t_{jk}^{a(m)} \exp(-\tau_b / \mu_k) + \exp(-\tau_a / \mu_j) t_{jk}^{b(m)} + \tilde{t}_{jl}^{a(m)} \otimes D_{ln}^{(m)} \otimes \tilde{t}_{nk}^{b(m)}. \end{aligned} \quad (\text{A15})$$

Eqs. (A12a), (A12b), (A13a) and (A15) constitute the adding/doubling equations. It should be pointed that the matrix associated with direct transmission is diagonal. In numerical computation, the numerical efficiency and accuracy can be improved substantially if the

multiplication of the direct transmission function with another quantity is evaluated analytically, such as

$$\Delta_{ij}^{(m)}(\tau) \otimes A_{jk}^{(m)} = \exp(-\tau / \mu_j) A_{jk}^{(m)}, \quad A_{jk}^{(m)} \otimes \Delta_{ki}^{(m)}(\tau) = A_{jk}^{(m)} \exp(-\tau / \mu_k). \quad (\text{A16})$$

As mentioned in preceding discussions, the continuous integration involved in adding/doubling calculation must be replaced by a proper quadrature scheme. Mathematically, we need to select proper pairs of  $(\mu_i, W_i)$  for the definition of the mathematical operator  $\otimes$  in Eqs. (A9a) and (A9b). The most popular quadrature schemes are Gauss, Lobatto, and Radau quadrature schemes [Press *et al.*, 1986; Hildebrand, 1974]. For the angular region involved, these three schemes cover  $\mu$  (or  $\mu'$ )  $\in (0,1)$ ,  $[0,1]$ , and  $(0,1]$ , respectively. That is, Gaussian quadrature is open at both ends, Lobatto quadrature is closed at both 0 and 1, and the Radau scheme is open at 0 but closed at 1. The radiance data at nadir view is usually required in retrieval applications. Thus, an extrapolation must be used to obtain the nadir-view radiance if Gaussian quadrature is used. Although the Lobatto scheme is closed at both ends of the integral region, the information at  $\mu=0$  actually does not make any contribution to the angular integration, as evident from Eqs.(A9a) and (A9b). In addition, including  $\mu=0$  will cause a singularity in the initialization of the adding/doubling calculation. Therefore, we use the Radau scheme in the present study.

To initialize the adding/doubling process, we start with a very thin homogeneous layer with optical depth  $\Delta\tau$  ( $\sim 10^{-8}$ ). The reflection and transmission truncation for this layer can be obtained on the basis of the invariance principle [Hansen and Travis, 1974] as follows:

$$\begin{aligned} r_{i,j}^{(m)} = & \frac{\tilde{\omega}\Delta\tau}{4\mu_i\mu_j} \left[ 1 - \frac{\Delta\tau}{2} \frac{\mu_i + \mu_j}{\mu_i\mu_j} \right] P_{i,j}^{r(m)} \\ & + \frac{\tilde{\omega}^2\Delta\tau^2}{32\mu_i\mu_j} \left[ (P_{ik}^{r(m)} / \mu_k) \otimes (P_{kj}^{t(m)} / \mu_k) + (P_{ik}^{t(m)} / \mu_k) \otimes (P_{kj}^{r(m)} / \mu_k) \right], \quad (\text{A17a}) \end{aligned}$$

$$t_{i,j}^{(m)} = \frac{\tilde{\omega}\Delta\tau}{4\mu_i\mu_j} \left[ 1 - \frac{\Delta\tau}{2} \frac{\mu_i + \mu_j}{\mu_i\mu_j} \right] P_{i,j}^{t(m)} + \frac{\tilde{\omega}^2\Delta\tau^2}{32\mu_i\mu_j} \left[ (P_{ik}^{t(m)} / \mu_k) \otimes (P_{kj}^{t(m)} / \mu_k) + (P_{ik}^{r(m)} / \mu_k) \otimes (P_{kj}^{r(m)} / \mu_k) \right]. \quad (\text{A17b})$$

In Eqs.(A17a) and (A17b),  $P_{ij}^{r(m)}$  and  $P_{ij}^{t(m)}$  are defined as follows

$$P_{ij}^{r(m)} = \sum_{l=m}^M (2 - \delta_{m0}) \tilde{\omega}_l \tilde{P}_l^m(-\mu_i) \tilde{P}_l^m(\mu_j) = \sum_{l=m}^M (2 - \delta_{m0}) \tilde{\omega}_l \tilde{P}_l^m(\mu_i) \tilde{P}_l^m(-\mu_j), \quad (\text{A18a})$$

$$P_{ij}^{t(m)} = \sum_{l=m}^M (2 - \delta_{m0}) \tilde{\omega}_l \tilde{P}_l^m(\mu_i) \tilde{P}_l^m(\mu_j), \quad (\text{A18b})$$

in which  $\tilde{\omega}_l$  is given by

$$\begin{aligned} \tilde{\omega}_l &= \frac{2l+1}{2} \int_{-1}^1 P(\mu) P_l(\mu) d\mu \\ &= \frac{2l+1}{2} \int_0^1 [P(\mu) + (-1)^l P(-\mu)] P_l(\mu) d\mu, \end{aligned} \quad (\text{A19})$$

where  $P(\mu)$  is phase function and  $P_l(\mu)$  is the Legendre polynomial of  $l$ th order. In numerical computation, we use the Radau quadrature scheme for the integration in Eq.(A19). Thus phase function information at the exact forward and backward directions is accounted for. The function  $\tilde{P}_l^m$  in Eqs.(A18a) and (A18b) are the “re-normalized” ( or the “normalized” called in DISORT [Stamnes *et al.* 2000]) associated Legendre polynomials first introduced by Dave and Armstrong [1970], defined as

$$\tilde{P}_l^m(\mu) = \sqrt{\frac{(l-m)!}{(l+m)!}} P_l^m(\mu), \quad (\text{A20a})$$

where  $P_l^m$  is the ordinary Legendre function. The normalized associated Legendre functions can be calculated on the basis of the following recurrence relationship:

$$\tilde{P}_{l+1}^m(\mu) = \frac{2l+1}{\sqrt{(l+m+1)(l-m+1)}} \mu \tilde{P}_l^m(\mu) - \sqrt{\frac{(l+m)(l-m)}{(l+m+1)(l-m+1)}} \tilde{P}_{l-1}^m(\mu), \quad (\text{A21a})$$

with the two initial values for the preceding recurrence given by

$$\tilde{P}_m^m(\mu) = (-1)^m \sqrt{\frac{(2m-1)!!}{(2m)!!}} (1-\mu^2)^{m/2}, \quad \tilde{P}_{m+1}^m(\mu) = \mu \sqrt{2m+1} \tilde{P}_m^m(\mu). \quad (\text{A21b})$$

Note that alternatives for initializing the preceding recurrence can be found in the paper by *Dave and Armstrong* [1970] and a technical report for DISORT [*Stamnes et al.* 2000]. It should be pointed out that in many references the phase function expansion based on Legendre polynomials is given in the form of

$$P^{(m)}(\mu_i, \mu_j) = \sum_{l=m}^M (2 - \delta_{m0}) \tilde{\omega}_l \frac{(l-m)!}{(l+m)!} P_l^m(\mu_i) P_l^m(\mu_j), \quad (\text{A22a})$$

where the associated Legendre polynomial or Legendre functions can be calculated on the basis of the following recursive relationship

$$P_{l+1}^m(\mu) = \frac{(2l+1)\mu P_l^m(\mu) - (l+m)P_{l-1}^m(\mu)}{l-m+1}. \quad (\text{A22b})$$

The factor  $(l-m)!/(l+m)!$  in Eq.(A22a) rapidly reduces to zero while the values of Legendre functions are very large for a large  $m$  with  $l \geq m$ , as noted by *Dave and Armstrong* [1970]. For this reason, the preceding approach given by Eqs.(A22a) and (A22b) for the expansion of the phase function in radiative transfer simulations is not numerically stable, in particular, when the asymmetry of phase function is substantial and higher order Legendre functions are required in the phase function expansion.

Since the predominant sizes of ice crystals in cirrus clouds are much larger than visible and near infrared wavelengths, there is a strong forward peak in the corresponding phase function. To include this forward peak in numerical computations, thousands of terms may be required in the Fourier expansions involved in Eqs.(A1a)-(A1c) for a general solar-

view geometry, and also in the phase function expansion given by Eqs. (A18a) and (A18b). It should be pointed that the number of radiance streams used in the adding/doubling calculation needs to increase with the increase of the terms used in the phase function expansion so that the orthogonality of the selected finite set of Legendre functions in a discrete form can be guaranteed. Thus, the strong forward peak makes the numerical computation impractical. For this reason, the strong forward peaks of phase functions are truncated in practice. The schemes used for the truncation are diverse, which have been evaluated in an extensive discussion by *Wiscombe*, [1977], who has further developed the  $\delta - M$  method in order to avoid the shortcomings pertaining to various ad hoc empirical approaches. For truncating the forward peak of the phase function involved in this study, we employ the method developed by *Hu et al.* [2000], which is an extension of the  $\delta - M$  method. After the phase function is truncated, the single-scattering properties need to be adjusted on the basis of the similarity principle [*Wiscombe*, 1977; *van de Hulst*, 1980; *Takano and Liou*, 1989b]. For example, optical depth and single scattering albedo are adjusted as follows:

$$\tau' = (1 - f\tilde{\omega})\tau, \quad \tilde{\omega}' = (1 - f)\tilde{\omega}/(1 - f\tilde{\omega}), \quad (\text{A23})$$

where  $f$  is the fraction of energy associated with the truncated forward peak.

## Acknowledgements

The authors thank Steve Platnick and Erik Olson for useful discussions during the course of this study. This research has been supported by a grant of NASA's MODIS project and partially by the Office of Naval Research. Heymsfield, McFarquhar, and Miloshevich's work was funded by NASA/EOS grant (contract No. S-97894-F).

## References

- Ackerman, S. A., W. L. Smith, J. D. Spinhirne and H. E. Revercomb, The 27-28 October 1986 FIRE IFO cirrus case study: Spectral properties of cirrus clouds in the 8-12  $\mu\text{m}$  window, *Mon. Wea. Rev.*, *118*, 2377-2388, 1990.
- Ackerman, S. A., K. I. Strabala, W. P. Menzel, R. A. Frey, C. C. Moeller, and L. E. Gumley, Discriminating clear sky from clouds with MODIS, *J. Geophys. Res.*, *103*, 32,141-32,157, 1998.
- Arnott, W. P., Y. Y. Dong, J. Hallett, and M. R. Poellot, Role of small ice crystals in radiative properties of cirrus: A case study, FIRE II, November 22, 1991, *J. Geophys. Res.*, *99*, 1371-1381, 1994.
- Baum B. A., D. Kratz, P. Yang, S. C. Ou, Y. X. Hu, P. F. Soulen, S. C. Tsay, Remote sensing of cloud properties using MODIS airborne simulator imagery during SUCCESS I. data and models, *J. Geophys. Res.*, 2000a (accepted and in press).
- Baum B. A., P. F. Soulen, K. I. Strabala, M. D. King, S. A. Ackerman, W. P. Menzel, P., Yang, Remote sensing of cloud properties using MODIS airborne simulator imagery during SUCCESS II. Cloud thermodynamic phase, *J. Geophys. Res.* 2000b (accepted and in press).
- Cox, C., and W. Munk, Measurement of the roughness of the sea surface from photographs of the sun's glitter, *J. Opt. Amer. Soc.*, *44*, 838-850, 1954.
- Cross, J. D., Study of the surface of ice with a scanning electron microscope. *Physics of Ice, Proceedings of the International Symposium on the Physics of Ice*, Munich, Germany, September 9-14, 1968. Plenum Press, New York, pp. 81-94, 1968.
- Dave, J.V. and B. Armstrong, Computations of high-order associated Legendre polynomials, *J. Quant. Spectrosc. Radiat. Transfer*, *10*, 557-562, 1970.

- Francis, P. N., Some aircraft observations of the scattering properties of ice crystals, *J. Atmos. Sci.*, 52, 1142-1154, 1995.
- Francis, P. N., A. Jones, R. W. Saunders, K. P. Shine, A. Slingo, Z. Sun, An observational and theoretical study of the radiative properties of cirrus: Some results from ICE'89, *Q. J. R. Meteor. Soc.*, 120, 809-848, 1994.
- Foot, J. S., Some observations of the optical properties of clouds: II. Cirrus, *Q. J. R. Meteor. Soc.*, 114, 145-164, 1988.
- Fu, Q., An accurate parameterization of the solar radiative properties of cirrus clouds for climate models, *J. Climate*, 9, 2058-2082, 1996.
- Gao, B. C. and Y. J. Kaufman, Selection of 1.375  $\mu\text{m}$  MODIS channel for remote sensing of cirrus clouds and stratospheric aerosols from space, *J. Atmos. Sci.*, 52, 4231-4237, 1995.
- Gayet, J. F., O. Crepel, and J. F. Fournol, A new polar nephelometer for in situ measurements of microphysical and optical properties of clouds, in *Proceedings of the Conference on Cloud Physics*, pp. 26-30, Am. Meteorol. Soc. Boston, Mass., 1995.
- Hansen, J. E., and J. B. Travis, Light scattering in planetary atmospheres, *Space Sci. Rev.*, 16, 527-610, 1974.
- Heymsfield, A. J. and C. M. R. Platt, A parameterization of the particle size spectrum of ice clouds in terms of the ambient temperature and the ice water content, *J. Atmos. Sci.*, 41, 846-855, 1984.
- Hildebrand, E. B., *Introduction to Numerical Analysis*, Dover Publications, New York, 1974.
- Hu, Y. X., and K. Stamnes, An accurate parameterization of the radiative properties of water clouds suitable for use in climate models. , *J. Climate*, 6, 728-742, 1993.

- Hu, Y. X., B. Wielicki, B. Lin and G. Gibson, Delta fit: A fast and accurate treatment of particle scattering phase functions with weighted singular-value decomposition least-square fitting, , *J. Quant. Spectrosc. Radiat. Transfer*, 65, 681-690, 2000.
- Hunt, G. E., and I. P. Grant, Discrete space theory of radiative transfer and its application to problems in planetary atmospheres, *J. Atmos. Sci.*, 26, 963-972, 1966.
- Inoue, T. On the temperature and effective emissivity determination of semi-transparent cirrus clouds by bispectral measurements in the 10  $\mu\text{m}$  region, *J. Meteorol. Soc. Japan*, 63, 88-99, 1985.
- King, M. D., Number of terms required in the Fourier expansion of the reflection function for optical thick atmospheres, *J. Quant. Spectrosc. Radiat. Transfer*, 30, 143-161, 1983.
- King, M. D., Y. J. Kaufman, W. P. Menzel, and D. Tanre, Remote sensing of cloud, aerosol, and water vapor properties from the Moderate Resolution Imaging Spectrometer (MODIS), *IEEE Trans. Geosci. Remote Sens.*, 30, 2-27, 1992.
- King, M. D., S.-C. Tsay, S. E. Platnick, M. Wang, and K. N. Liou, Cloud Retrieval algorithms for MODIS: Optical thickness, effective particle radius, and thermodynamic phase, MODIS Algorithm Theoretical Basis Document, 79pp., 1997, [available at <http://eospso.gsfc.nasa.gov/atbd/modistables.html>].
- Lenoble, J. Ed., *Radiative Transfer in Scattering and Absorbing Atmospheres: Standard Computational Procedures*. Deepak, Hampton, VA. 1985.
- Liou, K. N., Influence of cirrus clouds on weather and climate processes: A global perspective, *Mon. Wea. Rev.*, 114, 1167-1199, 1986.
- Liou, K. N., S. C. Ou, Y. Takano, F. P. J. Valero, and T. P. Ackerman, Remote sounding of the tropical cirrus cloud temperature and optical depth using 6.5 and 10.6  $\mu\text{m}$  radiometers during STEP, *J. Appl. Meteor.*, 29, 716-726, 1990.
- Mace, G. G., T. Ackerman, E. E. Clothiaux, and B. A. Albrecht, A study of composite cirrus morphology using data from a 94-GHz radar and correlations with

- temperature and large-scale vertical motion, *J. Geophys. Res.*, *102*, 13,581-13,593, 1997.
- Macke, A., J. Muller, and E. Rascke, Single-scattering properties of atmospheric crystals, *J. Atmos. Sci.*, *53*, 2813-2825, 1996.
- McFarquhar, G. M., and A. J. Heymsfield, Microphysical characteristics of three cirrus anvils sampled during the central equatorial pacific experiment (CEPEX), *J. Atmos. Sci.*, *52*, 4143-4158, 1996.
- McFarquhar, G. M., and A. J. Heymsfield, Parameterization of tropical cirrus ice crystal size distributions and implications for radiative transfer: Results from CEPEX, *J. Atmos. Sci.*, *54*, 2187-2200, 1997.
- Miloshevich, L. M., and A. J. Heymsfield, A balloon-borne continuous cloud particle replicator for measuring vertical profiles of cloud microphysical properties: Instrument design, performance, and collection efficiency analysis. *J. Atmos. Ocean. Tech.*, *14*, 753-768, 1997.
- Minnis, P., K. N. Liou, and Y. Takano, Inference of cirrus cloud properties using satellite-observed visible and infrared radiances, I. Parameterization of radiance fields, *J. Atmos. Sci.*, *50*, 1279-1304, 1993a.
- Minnis, P., K. N. Liou, and Y. Takano, Inference of cirrus cloud properties using satellite-observed visible and infrared radiances, II, Verification of theoretical cirrus radiative properties, *J. Atmos. Sci.*, *50*, 1305-1322, 1993b.
- Mitchell, D. L., S. K. Chai, Y. Liu, A. J. Heymsfield, Y. Dong, Modeling cirrus clouds: I. Treatment of bimodal size spectra and case study analysis, *J. Atmos. Sci.*, *53*, 2952-2966, 1996a.
- Mitchell, D. L., A. Macke, Y. Liu, Modeling cirrus clouds: II. Treatment of radiative properties of radiative properties, *J. Atmos. Sci.*, *53*, 2967-2988, 1996b.

- Mishchenko, M. I., W. B. Rossow, A. Macke A. A. Lacis, Sensitivity of cirrus cloud albedo, bidirectional reflectance and optical thickness retrieval accuracy to ice particle shape, *J. Geophys. Res.*, *102*, 16,973-16,985, 1996.
- Mishchenko, M. I., and A. Macke, Incorporation of physical optics effects and computation of the Legendre expansion for ray-tracing phase functions involving  $\delta$ -function transmission, *J. Geophys. Res.*, *103*, 1799-1805, 1998.
- Nakajima, T. and M. D. King, Determination of the optical thickness and effective particle radius of clouds from reflected solar radiation measurements. Part I: Theory, *J. Atmos. Sci.*, *47*, 1878-1893, 1990.
- Ohtake, T., Unusual crystals in ice frog, *J. Atmos. Sci.*, *27*, 509-511, 1970.
- Ou, S. C., K. N. Liou, W. M. Gooch, Y. Takano, Remote sensing of cirrus cloud properties using AVHRR 3.7 and 10.9  $\mu\text{m}$  channels, *Appl. Opt.*, *32*, 2171-2180, 1993.
- Posse, P. and W. von Hoyningen-Huene, Information about scattering properties and particle characteristics of a stratiform cloud at Helgoland by remote optical measurements, *Beitr. Phys. Atmos.*, *68*, 359-366, 1995.
- Press, W. H., B. P. Flannery, S. A. Teukolsky, and W. T. Vetterling, *Numerical Recipes*, 839pp., Cambridge University Press, New York, NY 1986.
- Rossow, W. B., and A. A. Lacis, Global seasonal cloud variations from satellite radiance measurements. II-cloud properties and radiative effects, *J. Climate*, *47*, 2488-2503, 1990.
- Stamnes, K., S.-C. Tsay, W. Wiscombe, and I. Laszlo, DISORT, a General-Purpose Fortran Program for Discrete-Ordinate-Method Radiative Transfer in Scattering and Emitting Layered Media: Documentation of Methodology (version 1.1), available at:  
[ftp://climate.gsfc.nasa.gov/pub/wiscombe/Multiple\\_Scatt/DISORT\\_1.2/DISORTReport.pdf](ftp://climate.gsfc.nasa.gov/pub/wiscombe/Multiple_Scatt/DISORT_1.2/DISORTReport.pdf), 2000.

- Stamnes, K., S.-C. Tsay, W. Wiscombe, and K. Jayaweera, Numerically stable algorithm for discrete-ordinate-method radiative transfer in multiple scattering and emitting layered media, *Appl. Opt.*, 27, 2502-2509, 1988.
- Stephens, G. L., S. C. Tsay, P. W. Stackhouse, and P. J. Flatau, The relevance of the microphysical and radiative properties of cirrus clouds to climate and climate feedback, *J. Atmos. Sci.*, 47, 1742-1753, 1990.
- Strabala, K. I., S. A. Ackerman, and W. P. Menzel, Cloud properties inferred from 8-12  $\mu\text{m}$  data, *J. Appl. Meteor.*, 2, 212-229, 1994.
- Sun, Z., and K. P. Shine, Studies of the radiative properties of ice and mixed-phase clouds, *Quart. J. Roy. Meteor. Soc.*, 120, 407-426, 1994.
- Takano, Y. and K. N. Liou, Radiative transfer in cirrus clouds. I Single-scattering and optical properties of hexagonal ice crystals, *J. Atmos. Sci.*, 46, 3-19, 1989a.
- Takano, Y. and K. N. Liou, Radiative transfer in cirrus clouds. II. Theory and computation of multiple scattering in an anisotropic medium, *J. Atmos. Sci.*, 46, 20-36, 1989b.
- Takano, Y., K. N. Liou, and P. Minnis, The effects of small ice crystals on cirrus infrared radiative properties, *J. Atmos. Sci.*, 49, 1487-1493, 1992.
- Twomey, S., Matrix methods for multiple scattering problems, *J. Atmos. Sci.*, 23, 289-296, 1966.
- van de Hulst, H. C., *Light Scattering by Small Particles*, Wiley, New York, 470pp, 1957.
- van de Hulst, H. C., *Multiple Light Scattering*. Academic Press, 739pp, 1980.
- Wielicki, B. A., J. T. Suttles, A. J. Heymsfield, R. M. Welch, J. D. Spinhire, M. L. C. Wu, and D. O. Starr, The 27-28 October 1986 FIRE IFO cirrus case study: Comparison of radiative transfer theory with observations by satellite and aircraft, *Mon. Wea. Rev.*, 118, 2356-2376, 1990.
- Wiscombe, W. J., The delta-M method: rapid yet accurate radiative flux calculations for strongly asymmetric phase functions, *J. Atmos. Sci.*, 34, 1408-1422, 1977.

- Wyser, K. and P. Yang, Average ice crystal size and bulk short-wave single-scattering properties of cirrus clouds, *Atmos. Res.*, 49, 315-335, 1998.
- Yang, P. and K. N. Liou, Light scattering by hexagonal ice crystals: Comparison of finite-difference time domain and geometric optics model, *J. Opt. Soc. Am. A*, 12, 162-176, 1995.
- Yang, P. and K. N. Liou, Geometric-optics-integral-equation method for light scattering by nonspherical ice crystals, *Appl. Opt.*, 35, 6568-6584, 1996.
- Yang, P., and K. N. Liou, Light scattering by hexagonal ice crystals: Solution by Ray-by-Ray integration algorithm, *J. Opt. Soc. Am. A*, 14, 2278-2289, 1997.
- Yang, P., and K. N. Liou, Single-scattering properties of complex ice crystals in terrestrial atmosphere, *Contrib. Atmos Phys.* 71, 223-248, 1998.

## Figure Captions

Figure 1a. Replicator images of ice crystals from a cirrus cloud observed on Nov. 25, 1991 during the FIRE-II field experiment. Note the three-layer structure with small quasi-spherical crystals in the top layer, and columns and bullet rosettes in the second layer. The third layer is composed mostly of large aggregated crystals.

Figure 1b. Same as Figure 1a, except that the observation was made on Dec. 5, 1991 and the top layer is dominated by pristine columns.

Figure 2a. Size distribution modeling the cirrus observed on Nov. 25, 1991 that is shown in Figure 1a. Panels A, B, and C show the size and habit distributions for the top, middle, and bottom layer, respectively. Panel D shows the mean size distribution averaged over height.

Figure 2b. Same as Figure 2a except for the case of Dec.5, 1991.

Figure 3. The mean size and single-scattering properties for the three-layer (Dec. 5, FIRE-II) cirrus model. The vertical lines indicate the results computed using the one-layer model mean size distribution (i.e., the cloud is assumed to be vertically homogeneous).

Figure 4. Phase function corresponding to the single-scattering properties shown in Figure 3.

Figure 5. The scattering angle versus solar zenith and view zenith angles for four azimuthal angles. Note that the scattering angles are essentially for side-scattering and backscattering directions.

Figure 6. The percent relative difference of bidirectional reflectance computed using the three- and one-layer models at MODIS 0.65  $\mu\text{m}$  band for thin cirrus ( $\tau=1$ ). The maximum difference for this case is about 5% and depends mainly on scattering angle.

Figure 7. Same as Figure 6 except for thick cirrus ( $\tau=10$ ).

Figure 8. Same as Figure 6 except for MODIS 2.11  $\mu\text{m}$  band. Note the relative difference is much higher (up to 12%) than at 0.65  $\mu\text{m}$  wavelength due to absorption by ice.

Figure 9. Same as Figure 7 except for MODIS 2.11  $\mu\text{m}$  band. The differences for large optical thickness reach up to 50% and depend also on viewing and solar zenith angles.

Figure 10. Comparison of the top and middle layer phase functions computed by assuming that the small “quasi-spherical” ice crystals are either spheres or non-spherical hexagons with an aspect ratio of unity. Note the presence of the ice sphere rainbow feature between  $130^\circ$  and  $140^\circ$ .

Figure 11. The percent relative difference of the bidirectional reflectances computed assuming spherical and hexagonal shapes for the small “quasi-spherical” ice crystals. The difference contours shown are for thin cirrus ( $\tau=1$ ) at MODIS 2.11  $\mu\text{m}$  band. Note the large differences at the ice rainbow and backscattering angles.

Figure 12. Same as Figure 11 except for thick cirrus ( $\tau=10$ ). Note the smoothing of the rainbow maximum.

Figure 13. Same as Figure 11 except for MODIS 0.65  $\mu\text{m}$  band. Note the absence of the positive backscattering angle maximum.

Figure 14. Same as Figure 13 except for thick cirrus ( $\tau=10$ ).

Table 1. The single scattering properties of the top and middle layers, which are computed in conjunction with two assumptions for the shapes of the “quasi-spherical” small ice crystals ( ice spheres and hexagons with aspect ratio of 1). Note that the shapes of ice crystals with size larger than 50  $\mu\text{m}$  are assumed to be unchanged .

	$\lambda=0.65 \mu\text{m}$		$\lambda=2.11 \mu\text{m}$	
	Spheres for “quasi- spherical” particles	Hexagons for “quasi- spherical” particles	Spheres for “quasi- spherical” particles	Hexagons for “quasi- spherical” particles
<u>Top layer</u>				
$\beta_e$ (1/km)	0.32207	0.36926	0.33092	0.36005
$\tilde{\omega}$	0.99999	0.99999	0.91208	0.91335
$g$	0.83271	0.77965	0.86188	0.80258
$f_{\delta}$	0.070293	0.11689	0.038339	0.035189
<u>Middle layer</u>				
$\beta_e$ (1/km)	0.41679	0.42553	0.41837	0.42446
$\tilde{\omega}$	0.99998	0.99998	0.85099	0.85187
$g$	0.81627	0.80842	0.87949	0.86934
$f_{\delta}$	0.12765	0.13488	0.087641	0.086295

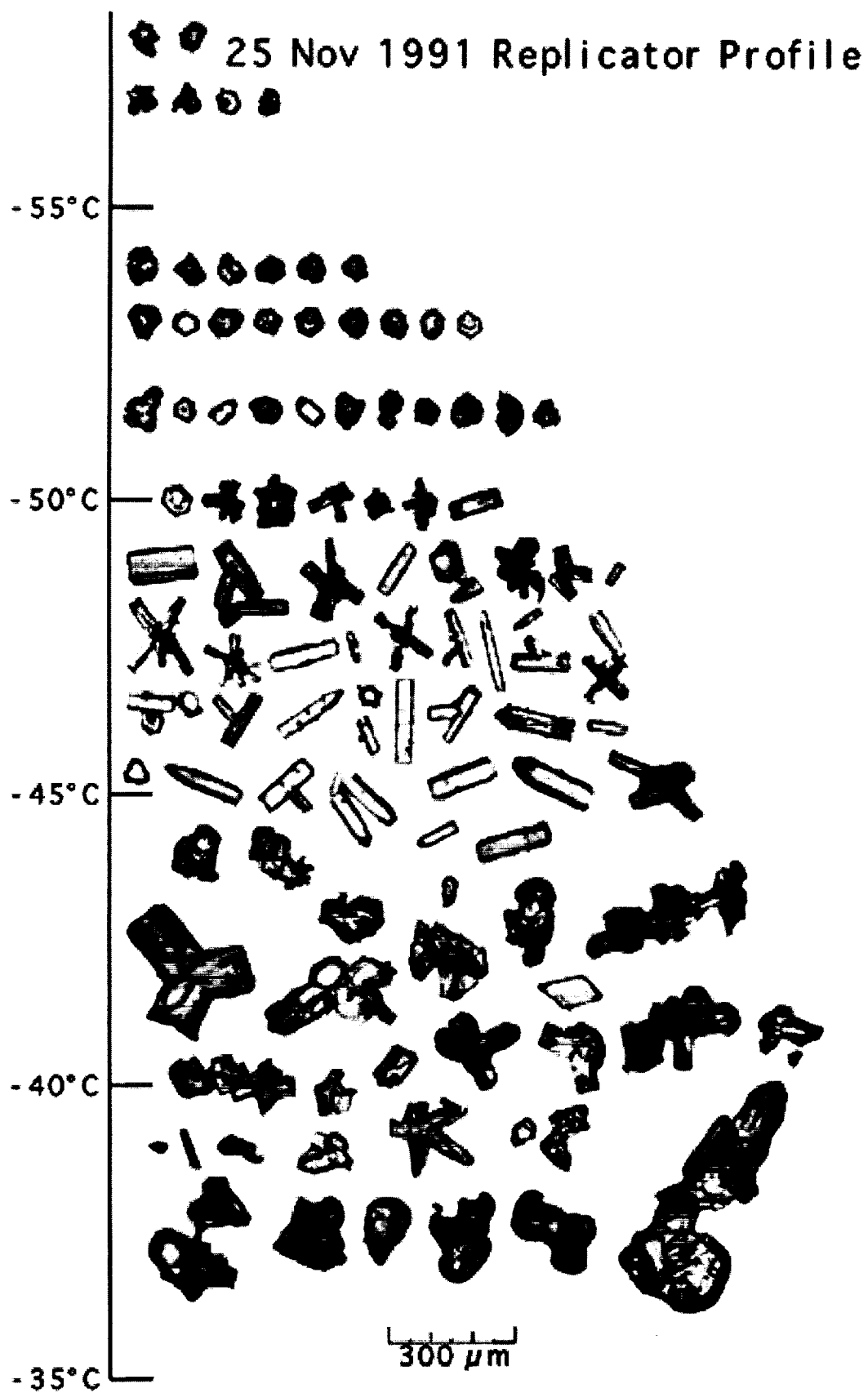
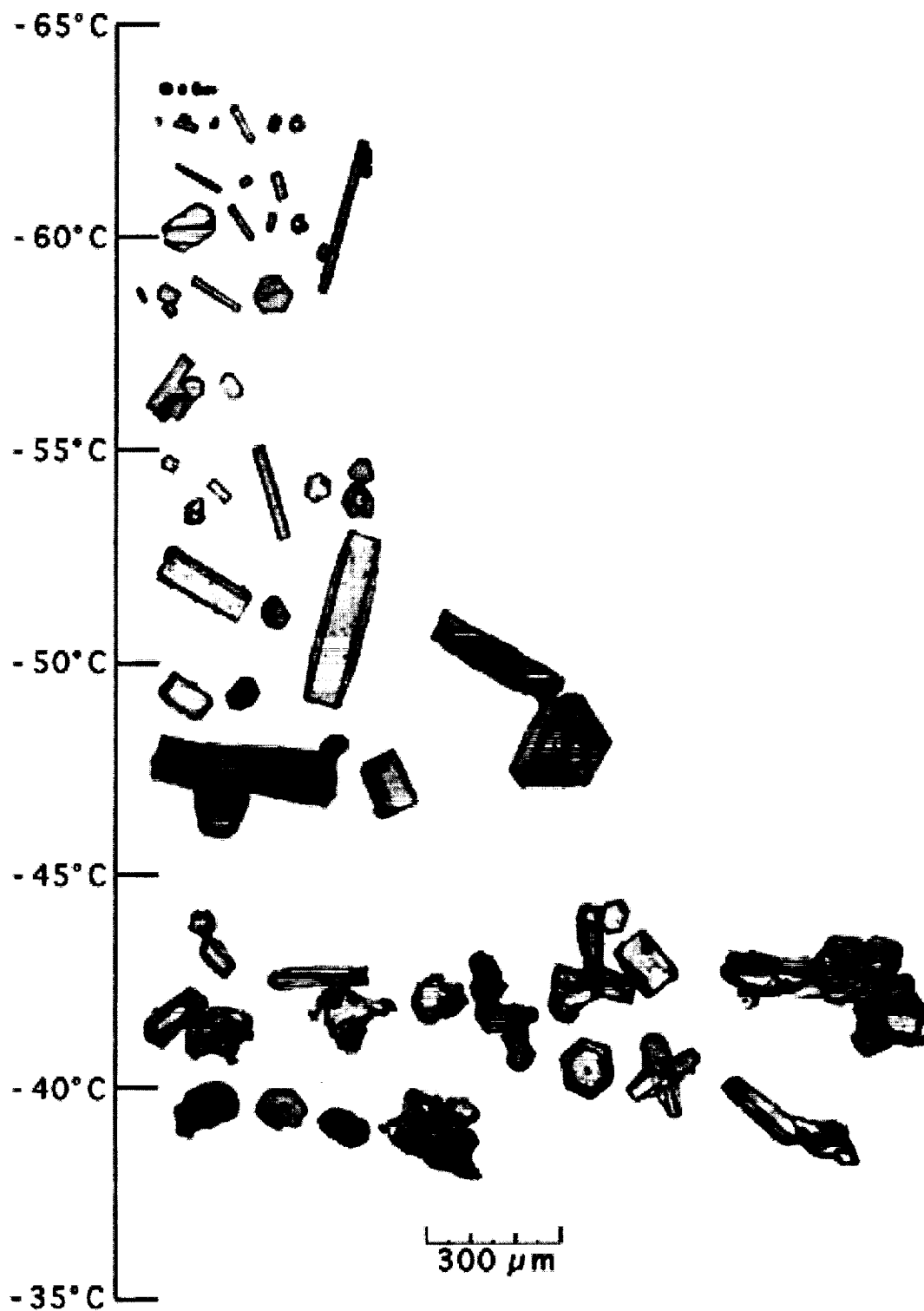


Fig. 1a

# 5 Dec 1991 Replicator Profile



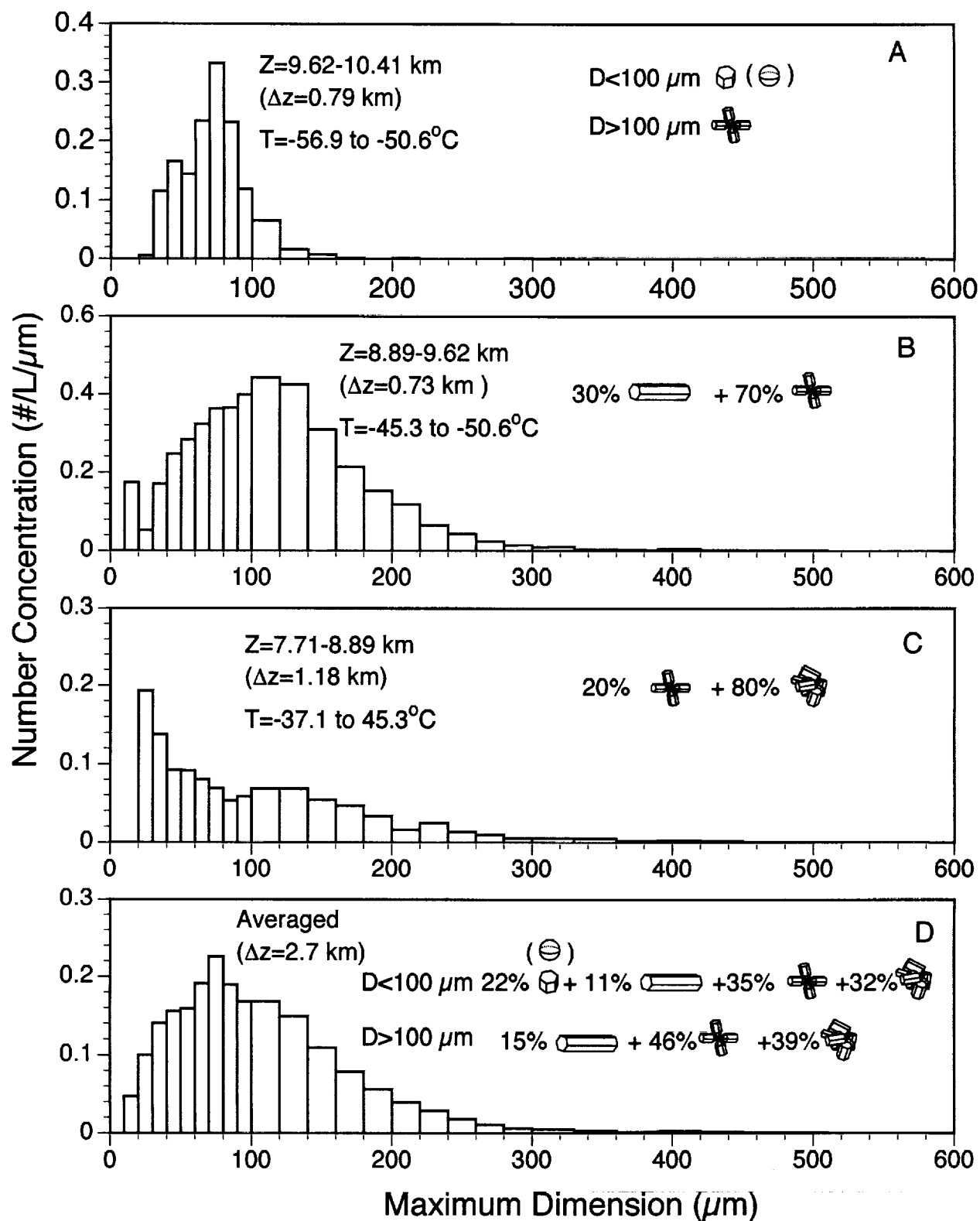


Fig.2a

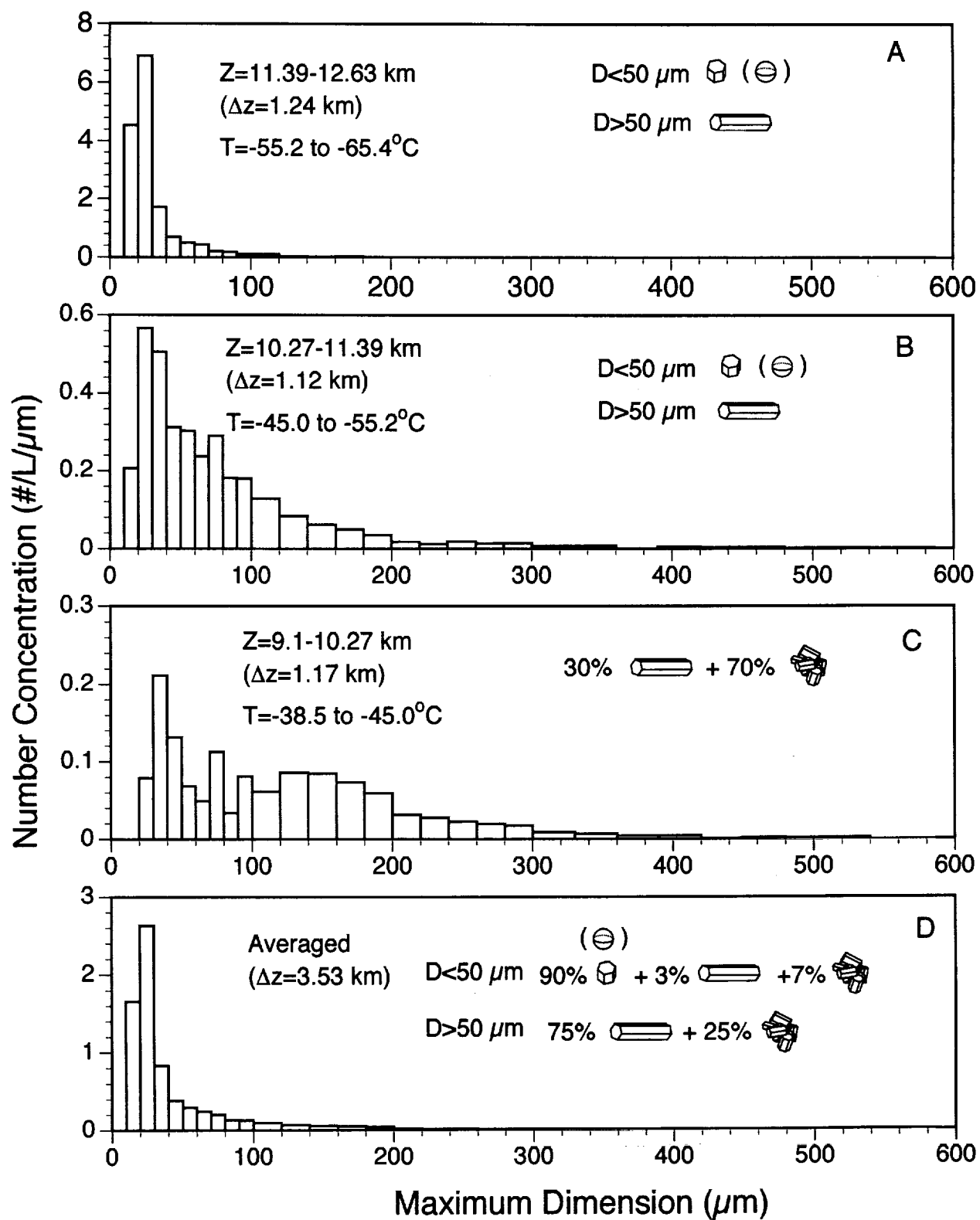


Fig.2b

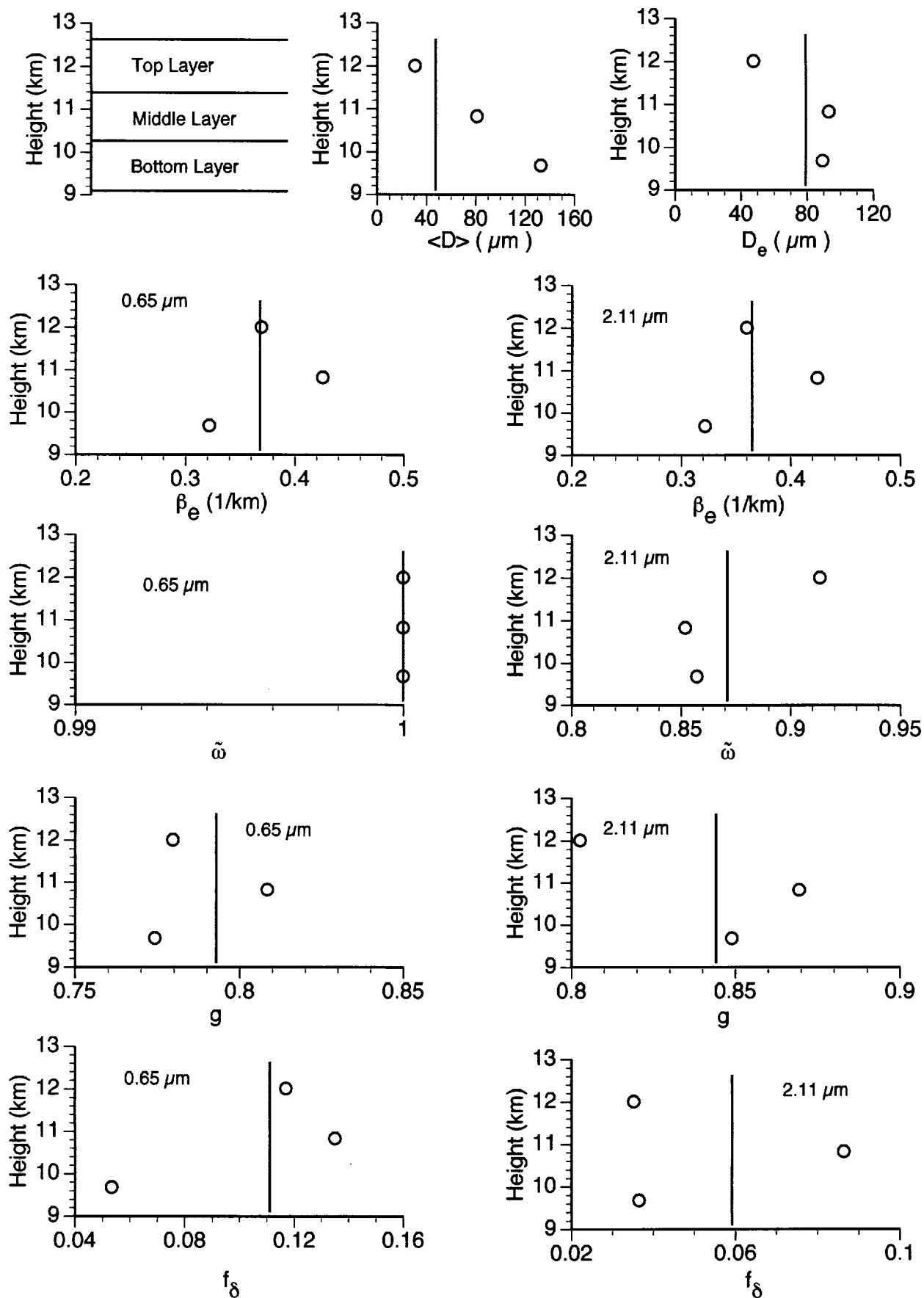


Fig.3

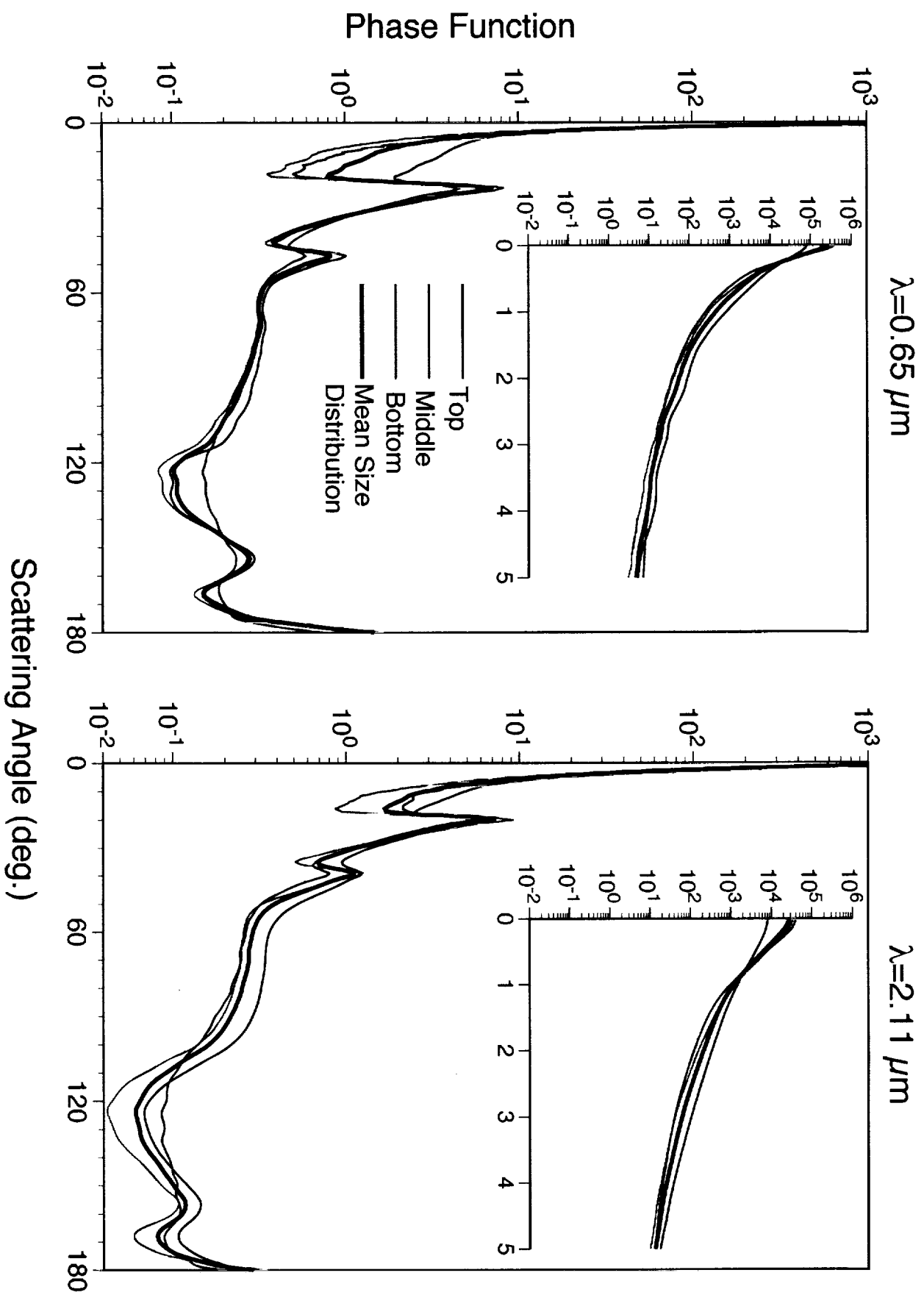


Fig.4

## Contours of Scattering Angle

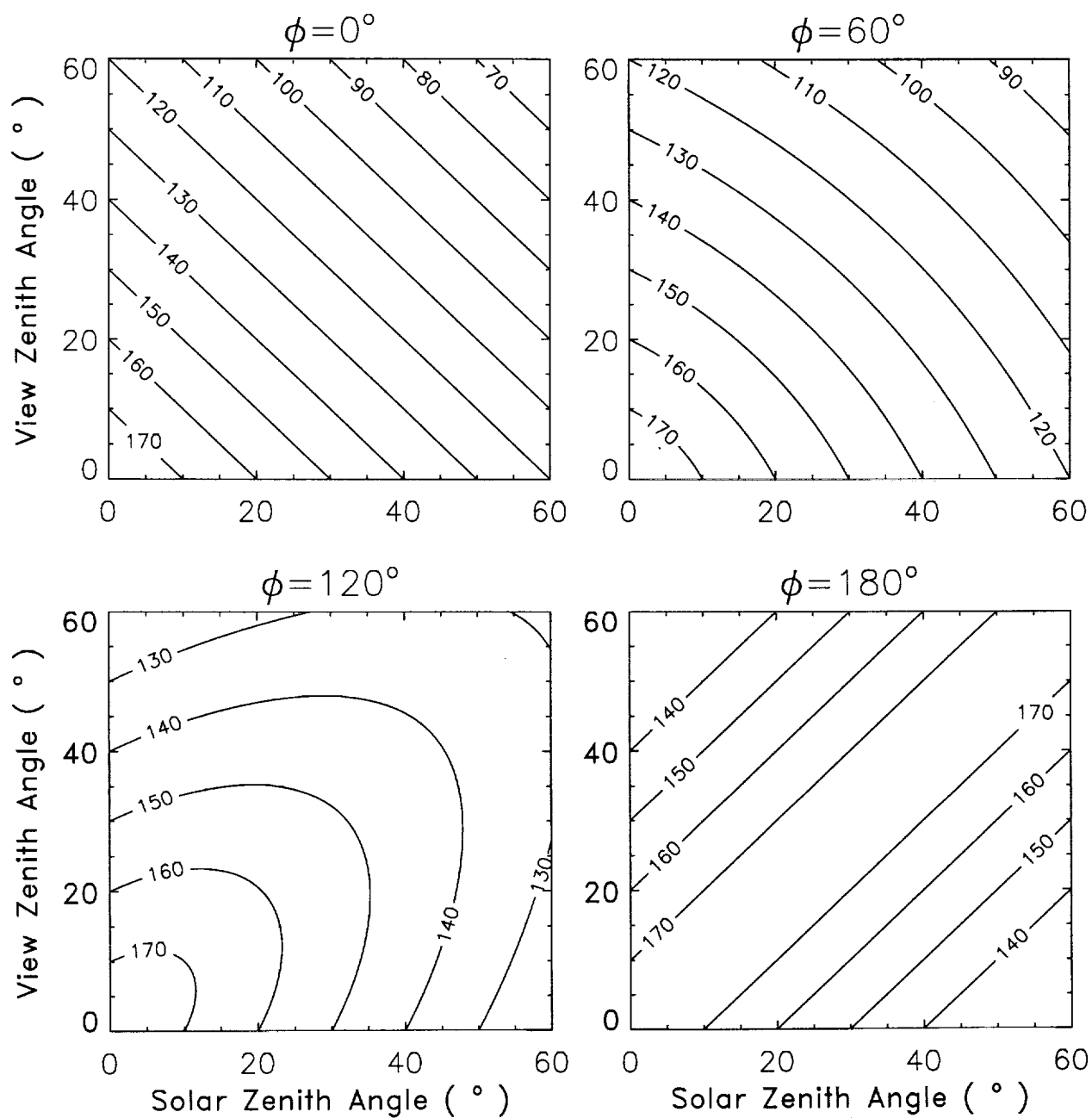


Fig.5

$\lambda=0.65 \text{ } \mu\text{m}$ , Thin Cirrus ( $\tau=1$ )

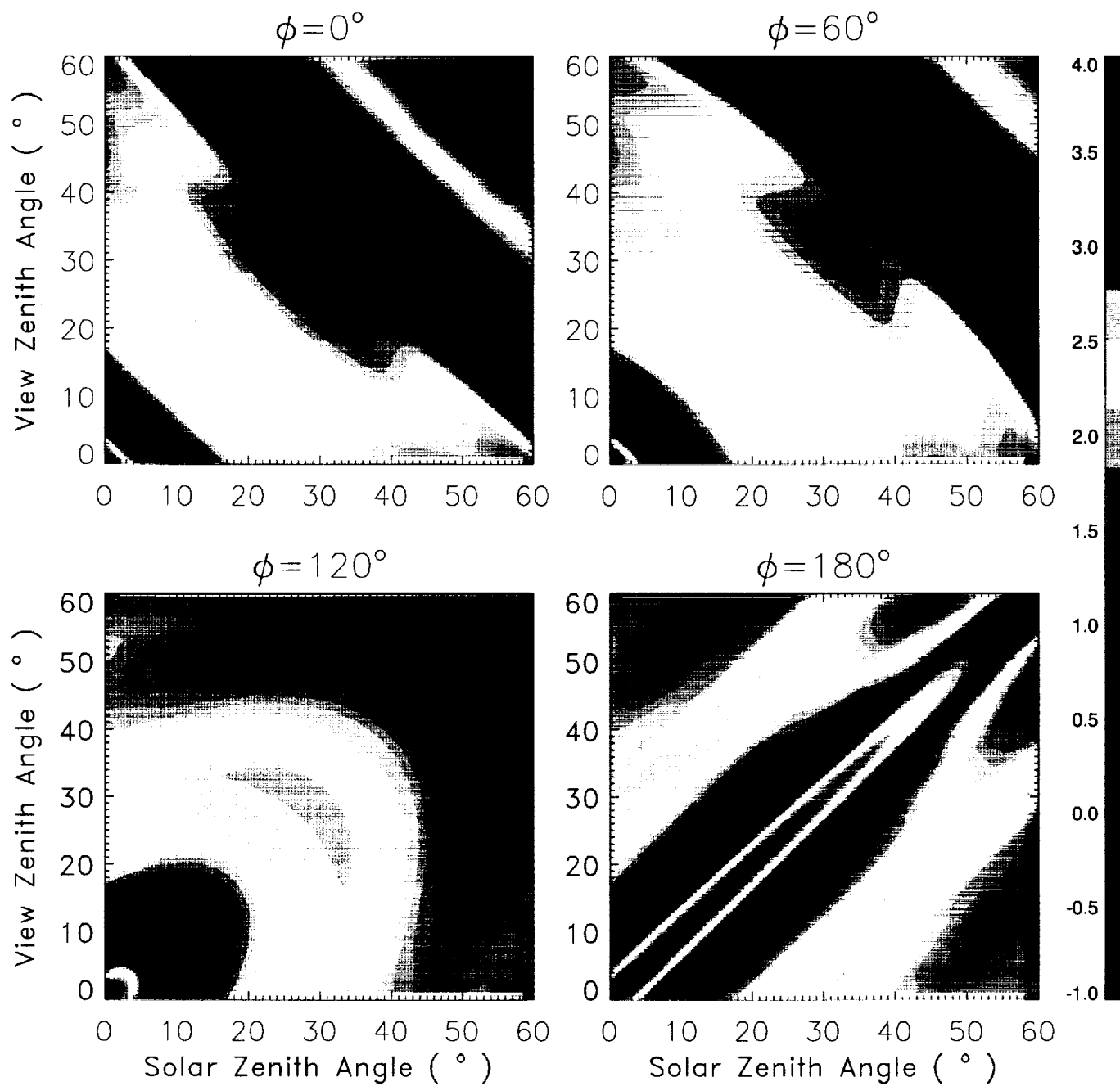


Fig.6

$\lambda=0.65 \text{ } \mu\text{m}$ , Thick Cirrus ( $\tau=10$ )

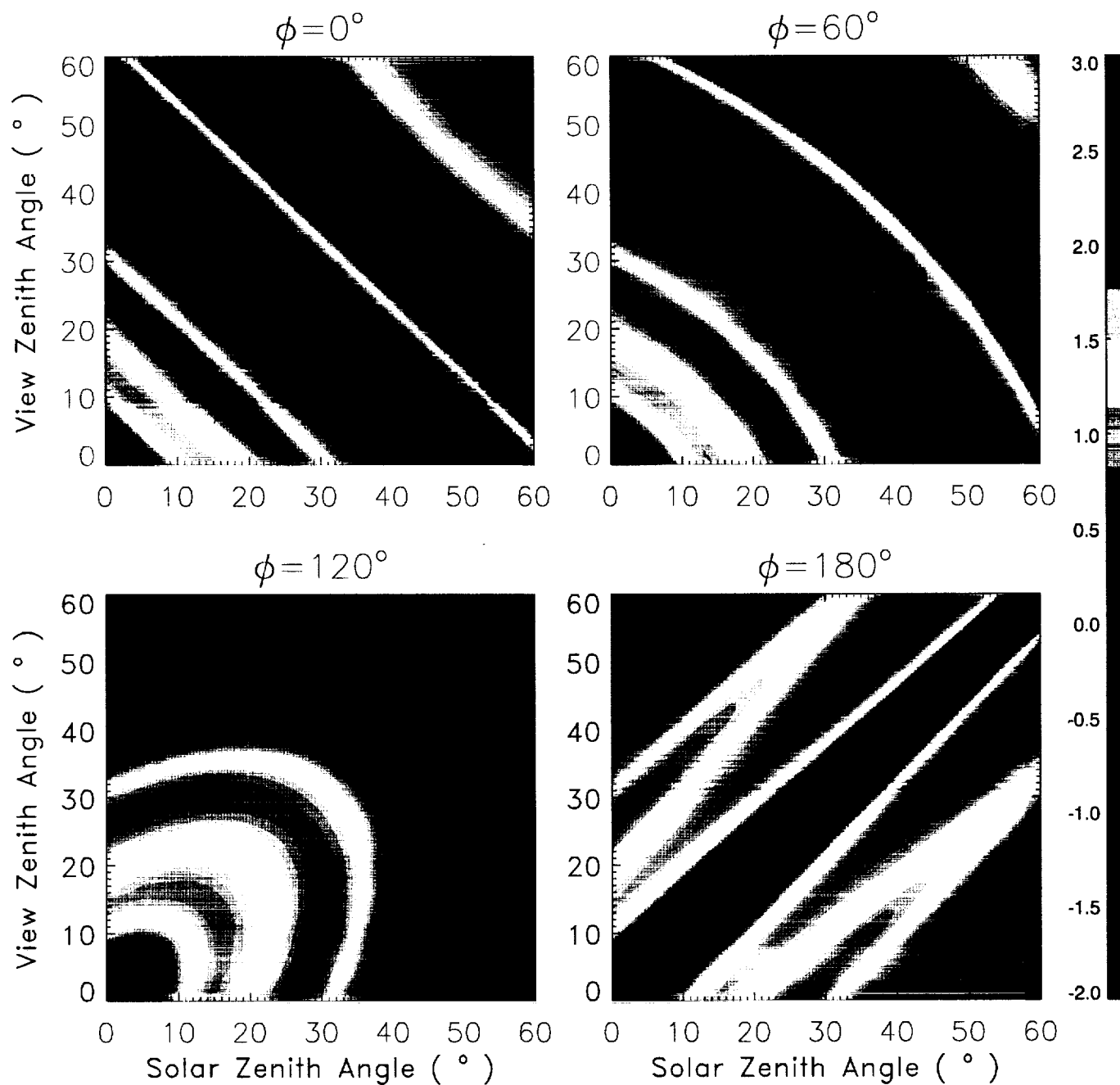


Fig.7

$\lambda=2.11 \text{ } \mu\text{m}$ , Thin Cirrus ( $\tau=1$ )

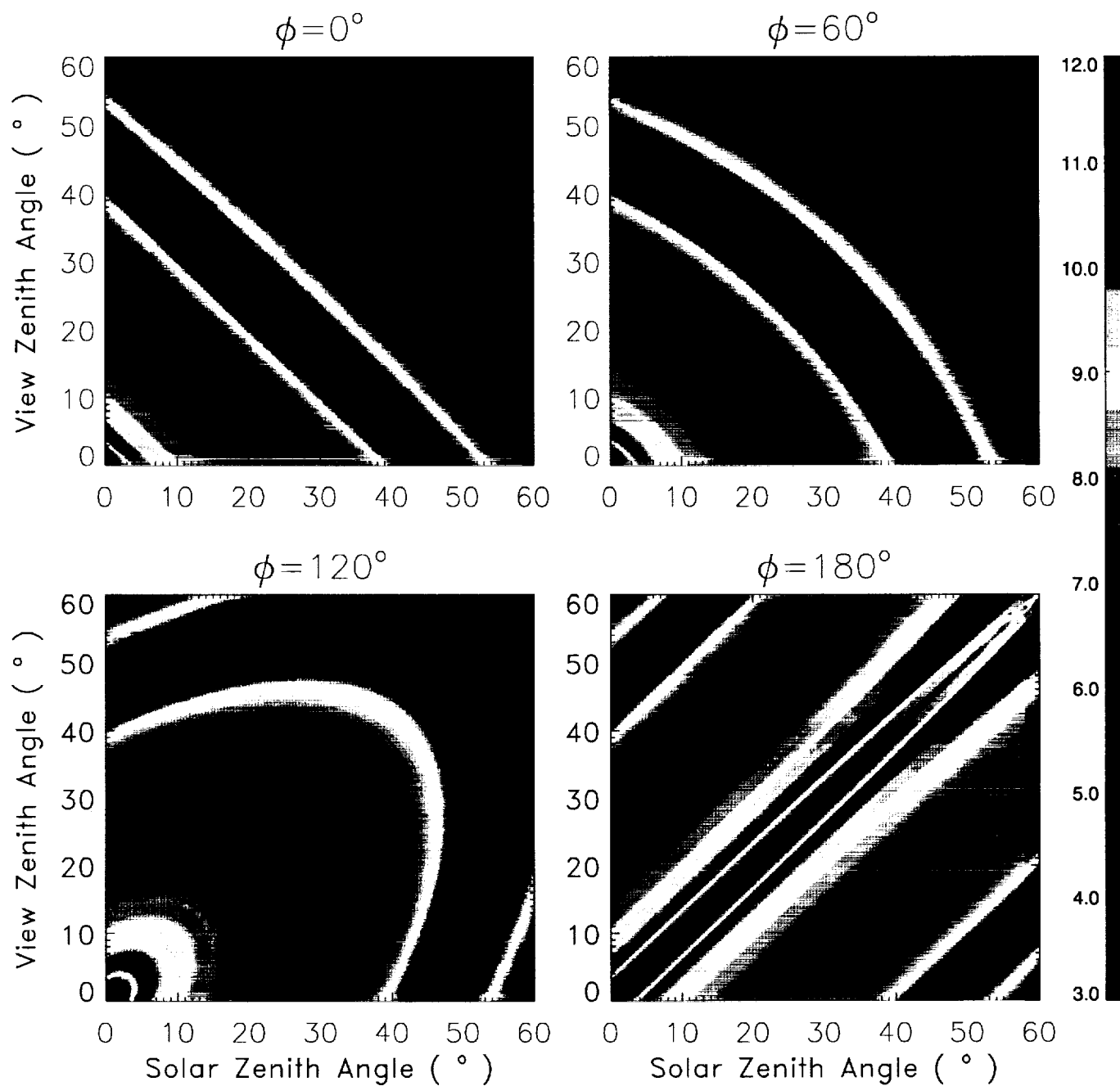


Fig.8

$\lambda=2.11 \text{ } \mu\text{m}$ , Thick Cirrus ( $\tau=10$ )

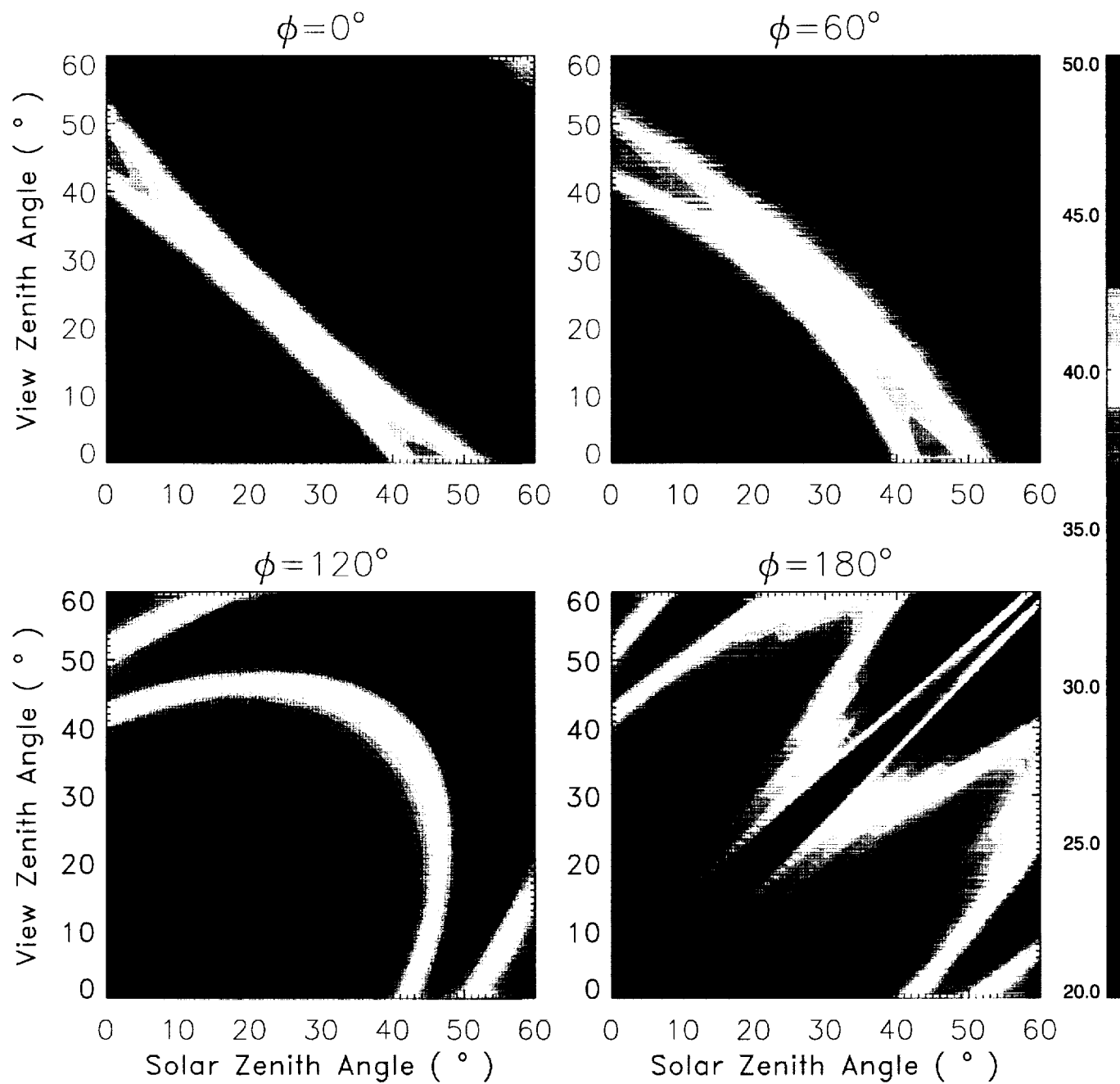


Fig.9

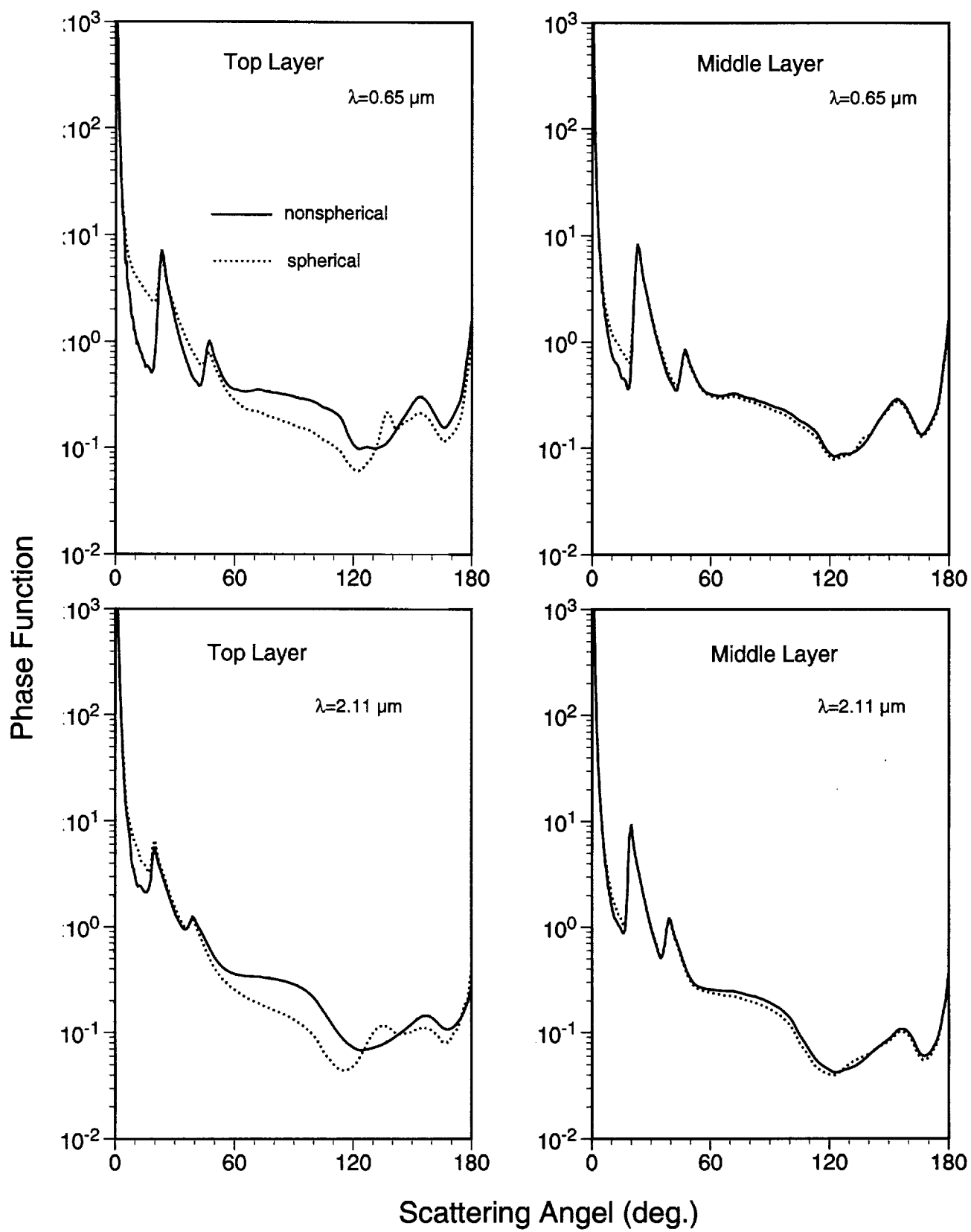


Fig.10

$\lambda=2.11 \text{ } \mu\text{m}$ , Thin Cirrus ( $\tau=1$ )

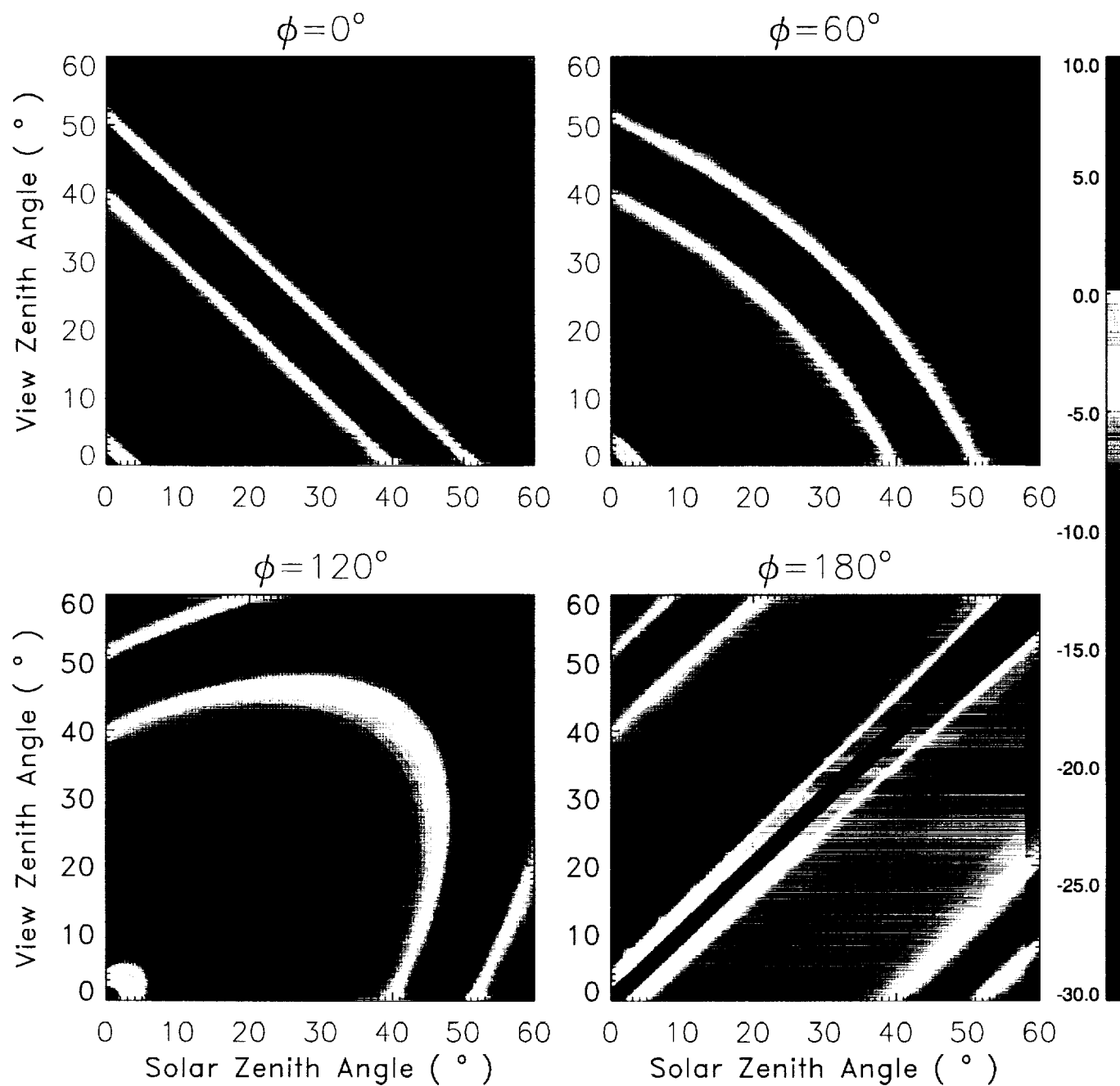


Fig.11

$\lambda=2.11 \text{ } \mu\text{m}$ , Thick Cirrus ( $\tau=10$ )

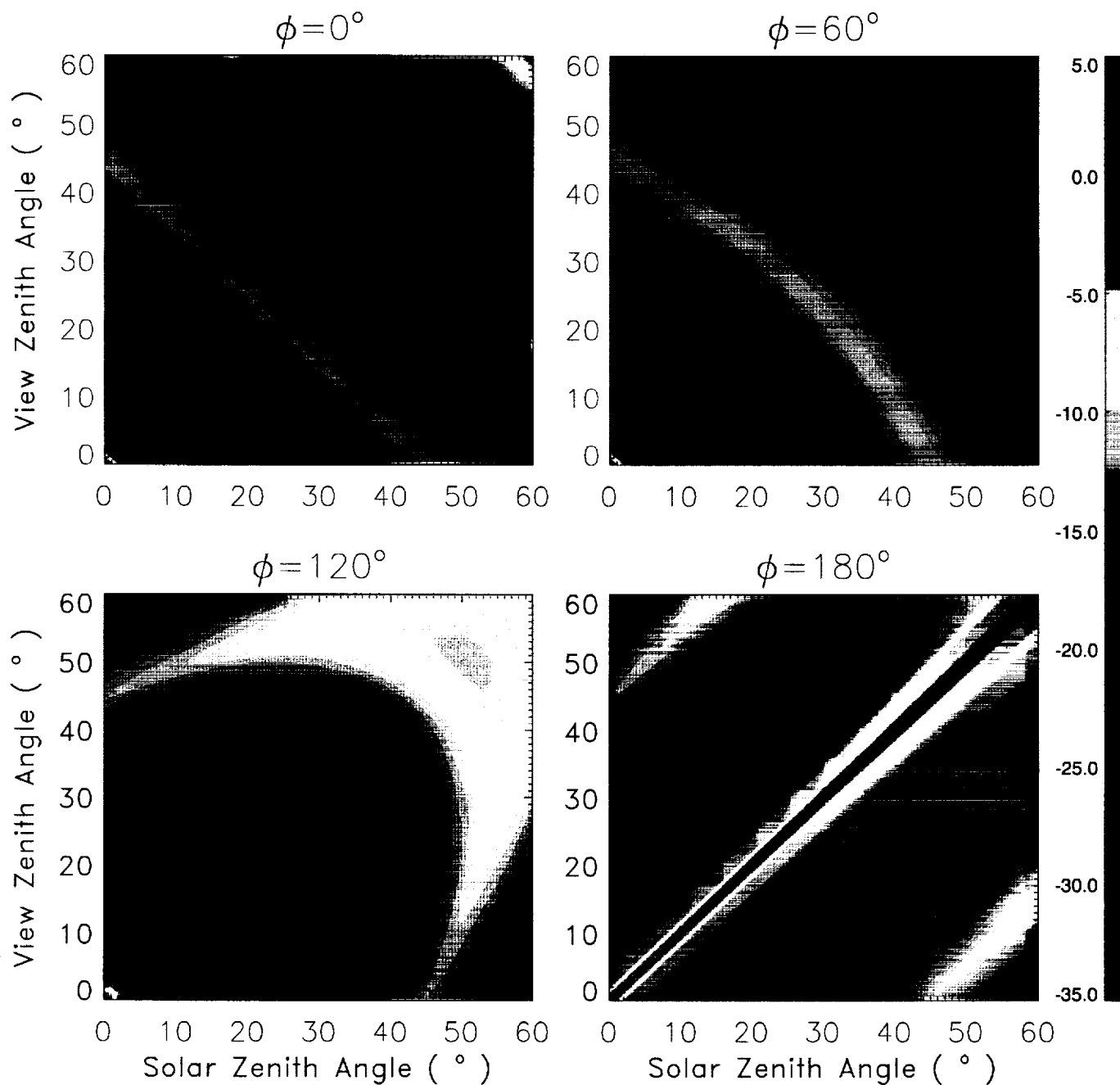


Fig.12

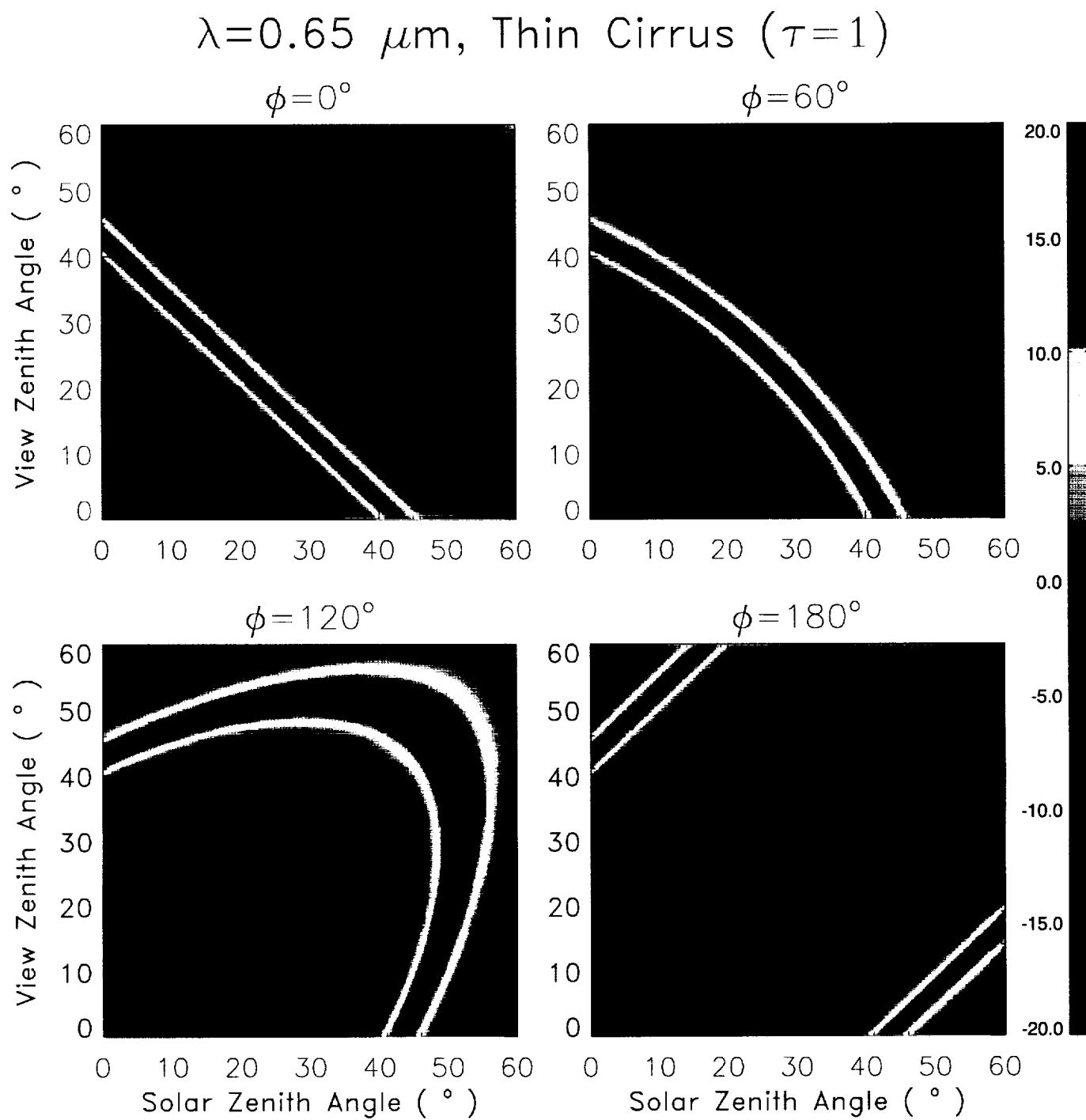


Fig.13

$\lambda=0.65 \text{ } \mu\text{m}$ , Thick Cirrus ( $\tau=10$ )

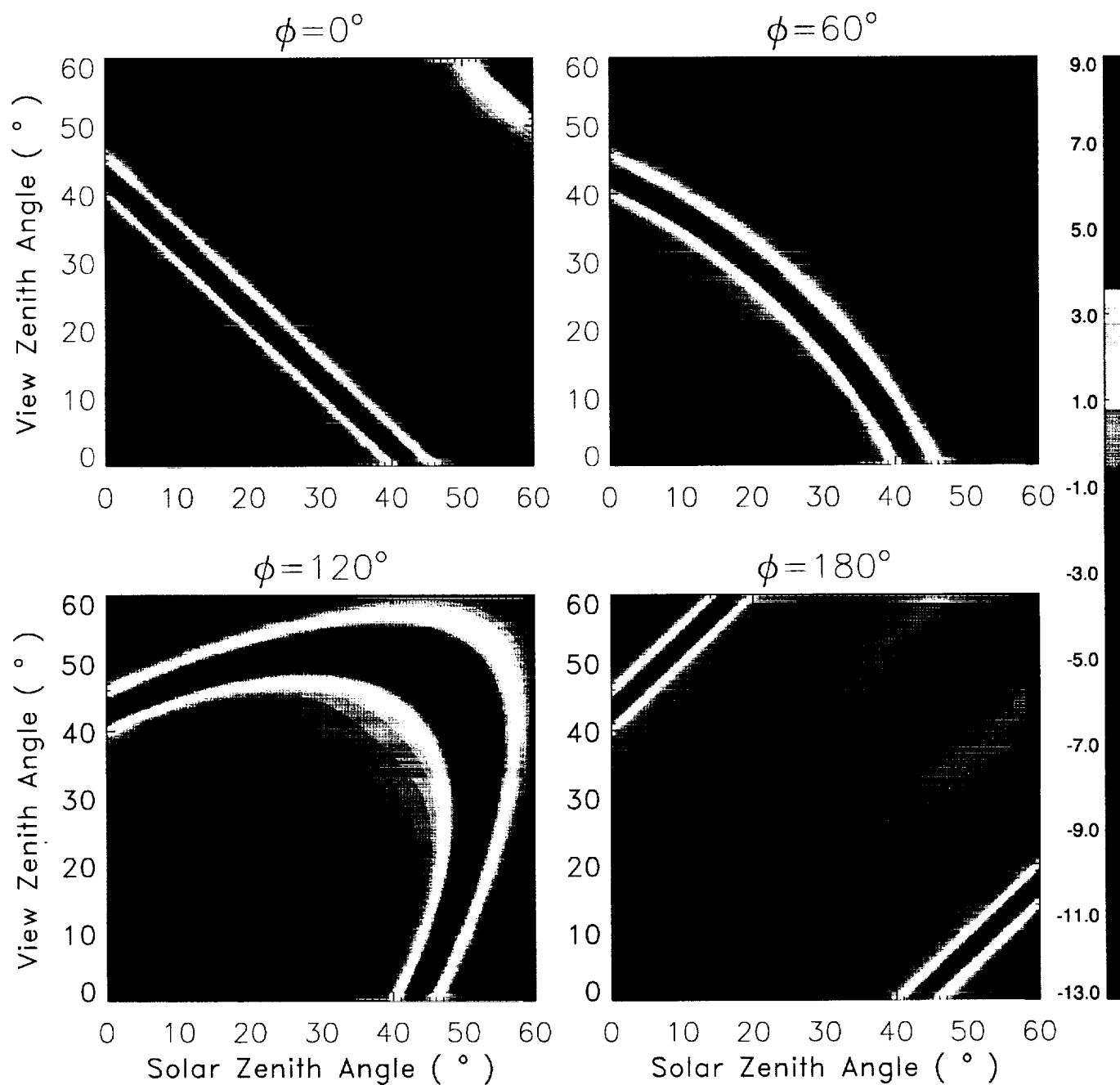


Fig.14

## Sensitivity of Cirrus Bidirectional Reflectance at MODIS Bands to Vertical Inhomogeneity of Ice Crystal Habits and Size Distributions

P. Yang<sup>1</sup>, B.-C. Gao<sup>2</sup>, B. A. Baum<sup>3</sup>, W. Wiscombe<sup>4</sup>, Y. Hu<sup>3</sup>, S. L. Nasiri<sup>5</sup>, P. F. Soulen<sup>6,4</sup>, A. J. Heymsfield<sup>7</sup>, G. M. McFarquhar<sup>7</sup>, L. M. Miloshevich<sup>7</sup>

1. Scientific Systems and Applications, Inc., Lanham, MD
2. Remote Sensing Division, Naval Research Laboratory, Washington, D.C.
3. NASA Langley Research Center, Hampton, VA
4. NASA Goddard Space Flight Center, Greenbelt, MD
5. Cooperative Institute for Meteorological Satellite Studies/University of Wisconsin, Madison, WI
6. Joint Center for Earth Systems Technology, University of Maryland Baltimore County, Baltimore, MD
7. National Center for Atmospheric Research, Boulder, CO

---

*Corresponding author address:* Dr. Ping Yang, Code 913, NASA Goddard Space Flight Center, Greenbelt, MD 20771; Tel: 301-614-6238; Fax: 301-614-6307; email: [pyang@climate.gsfc.nasa.gov](mailto:pyang@climate.gsfc.nasa.gov).